THE THEORY AND APPLICATION OF BIPOLAR TRANSISTORS AS DISPLACEMENT DAMAGE SENSORS

By

Andrew Michael Tonigan

Thesis

Submitted to the Faculty of the

Graduate School of Vanderbilt University

in partial fulfillment of the requirements

for the degree of

MASTER OF SCIENCE

in

INTERDISCIPLINARY MATERIALS SCIENCE

May, 2017

Nashville, Tennessee

Approved:

Ronald D. Schrimpf, Ph.D.

D. Greg Walker, Ph.D.

To the fond memories of my mother, Diane, my father, Eric,

my grandmother, June, and my grandfather, Richard.

ACKNOWLEDGEMENTS

TABLE OF CONTENTS

Page

LIST OF TABLES

LIST OF FIGURES

NOMENCLATURE/ACRONYMS

AmBe	americium-beryllium
ASTM	formerly "American Society for Testing and Materials"
ACRR	annular core research reactor
B_4C	boron carbide
BJT	bipolar junction transistor
Bq	becquerel (disintegrations/second)
Ca-252	californium-252
COTS	commercial off-the-shelf
CYR	charge yield ratio
DDF	displacement damage factor
DUT	device under test
ELDRS	enhanced low dose rate sensitivity
f_T	transistor cut-off frequency
HEDP	high energy density physics
ISDE	Institute for Space and Defense Electronics
I-V	current-voltage
keV	kilo-electron volt
krad(A)	kilorad – unit of absorbed dose in material "A"
LB-44	44-inch-long lead-boron bucket
MeV	mega-electron volt
MHz	mega-hertz (frequency)
MJ	megajoule
mA	milli-amphere
μm	micrometer
MRED	Monte Carlo Radiative Energy Deposition code
MW	megawatts
n	electron concentration in conduction band
NAA	neutron activation analysis
NIEL	non-ionizing energy loss
NIST	National Institute of Standards and Technology
NPN	doping polarity with n-type and p-type semiconducting material
Φ_p	particle fluence (particles per cm_2)
p	hole concentration in the valence band
Pb	lead
PKA	primary knock-on atom
RBS	Rutherford back-scattering
SNL	Sandia National Laboratories
SRH	Shockley-Read-Hall
τ	minority carrier lifetime
TA-V	Technical Area V
T_d	displacement threshold energy
TLD	thermoluminescent dosimeter
TID	total ionizing dose
UO_2-BeO	uranium dioxide – beryllium oxide
V	volts
VU	Vanderbilt University

Chapter I: Introduction

Electronic systems enhance our ability to explore, observe, and operate in extreme environments. Extreme environments that make the reliability of electronics an issue, and where precision is of great importance, include neutron and proton radiation environments. Intense neutron radiation occurs in and around nuclear reactors and could arise in military conflict [1]. Intense proton radiation occurs in the orbital space environment and can be created by particle accelerators of all types (i.e. medical, industrial and scientific) [2]. Understanding the performance of electronic systems and their components in laboratory-based environments is imperative to predicting their performance in operational radiation environments.

The characteristics of laboratory-based radiation sources can vary significantly and consistent measurement techniques for characterizing the particle fluence (integral of particle flux, total number of particles/cm^2) received by the device under test (DUT) are necessary. Presented in this thesis are proof of concept examples of how to use a specific electronic component -the bipolar junction transistor- as a particle radiation sensor for measuring atomic displacement damage. Previously, this technique has had a limited measurement range but offers benefits over traditional techniques [3]. This work sets out to demonstrate its use over a wide range of neutron fluences and evaluate its application for measuring proton fluences.

The use of bipolar junction transistors (BJTs) as displacement damage sensors was established as a standard technique in the early 1990s by Kelly & Griffin [3]. The methodology of utilizing transistors as displacement damage sensors was originally applied to:

- Provide a useful displacement damage metric for environments where the neutron spectrum is difficult to characterize or in which a test object will significantly perturb the neutron spectrum;

- Improve the determination of neutron spectra in the important 0.5-3 MeV energy region when fission foils cannot be easily used and where other activation sensors fail to exhibit adequate response [3].

The BJT damage methodology was shown to be an effective means of quantifying neutron fluence as an 1-MeV damage equivalent neutron fluence in silicon (1-MeV(Si) n/cm^2), a widely used metric when pursuing device performance qualification and quantifying neutron displacement damage [4]. The use of device response for displacement damage measurement is standardized in test method ASTM E1855, Standard Test Method for Use of 2N2222A Silicon Bipolar Transistors as Neutron Spectrum Sensors and Displacement Damage Monitors [5]. The use of this test method is particularly favorable when the results of the experiment will be used in the verification and validation of device performance models. This method offers a less expensive and minimally invasive means to measuring neutron displacement damage and presents significant advantages over performing a full spectral characterization of a neutron environment using neutron activation analysis (NAA) [6]. Increasing the sensitive fluence range of this method is important for displacement damage testing at High Energy Density Physics (HEDP) facilities, like the Z-Machine [7] and National Ignition Facility [8], for which typical neutron fluences are below the lower threshold of the current standard ASTM E1855-15 test method.

The methodology of ASTM E1855 relies on the Messenger-Spratt equation presented below [9]. Originally derived in 1958, the Messenger-Spratt equation indicates

a linear proportionality between the change in the reciprocal gain (or increase in base current at fixed collector current) and the incident particle fluence for a given spectrum/energy in BJTs:

$$\frac{1}{\beta_{post}} - \frac{1}{\beta_0} = \frac{K_1 \Phi_p}{f_T} = \frac{\Delta I_B}{I_{C,1\,mA}} \tag{1}$$

where β_0 is the initial gain, β_{post} is the gain after the irradiation, K_1 is an empirically derived damage factor, f_T is the cut-off frequency, Φ_p is the particle fluence, $I_{C,1\,mA}$ is the collector current fixed at 1 mA, and ΔI_B is the excess base current. While this form of the Messenger-Spratt equation provides the theoretical basis for the application of a particular transistor as a sensor, it also lends insight into how to predict the sensitivity of different transistors. This is captured in the transistor cut-off frequency, f_T on the right-hand side of the equation. The Messenger-Spratt equation indicates that the reciprocal of the cut-off frequency will be proportional to the change in reciprocal current gain. This proportionality is a consequence of the variation of f_T with transistor base width. Therefore, a transistor with lower f_T will experience a larger change for the same fluence, i.e., be more sensitive to displacement damage. The transistors used in this work have f_T ranging from 1.2 MHz to 300 MHz. The 1.2 MHz transistor, the 2N1486, performs with the increased sensitivity to displacement damage needed for use at HEDP facilities [10]. In addition to the interest in displacement damage from neutron radiation sources, displacement damage from proton radiation has been found to be important in a common application environment, the satellite orbitals around the Earth [2]. For this reason, the correlation between proton and neutron irradiation is of scientific interest.

The experiments performed at proton and neutron radiation sources during this thesis reveal advantages and disadvantages when seeking to investigate displacement

damage from either source. Proton irradiation facilities provide a single particle energy and can be operated inexpensively in a controlled manner (rapid on/off, controlled flux). However, these facilities usually require samples to be exposed under vacuum, have small uniform exposure areas, and they do not include the broad spectrum of proton energies usually encountered in operational space and high altitude environments.

Neutrons can be experimentally produced by either fission, fusion, radioactive decay or spallation. With nuclear fission and fusion reactors there can be repeatability issues due to the stochastic nature of nuclear chain reactions, especially with HEDP experiments. However, the neutron radiation spectrum can be tailored to approximate the operational environment spectrum and reactor facilities can allow for large areas of uniform irradiation conditions. Radioactive neutron sources include californium-252, which undergoes spontaneous fission, and americium-beryllium that produce neutrons via the (α,n) nuclear reaction. These sources typically have low neutron flux (<10^2 n/cm^2-s at testing positions for AmBe [12] and <10^8 n/cm^2-s for Ca-252 [13]) and require lengthy irradiation times to reach a significant fluence level. In the case of spallation, benefits and drawbacks are similar to that provided by proton accelerators [11]. In all neutron irradiations, materials used in testing will experience some degree of neutron activation and require radiation protection precautions, which can delay experimenter access.

The prevalence of nuclear reactors and the vast database established in the investigation of nuclear weapons effects made neutron displacement damage testing more advantageous in the past [14]. However, increased safety regulations, the closure of many research reactors [15], and, in recent years, the cost effectiveness have increased the favorability of using ion beams [16] and proton radiation testing [17].

Regardless, the optimal particle radiation source is that which is present in the actual application environment.

The specific aims of this thesis are twofold:

- Provide evidence for the use of the 2N1486 transistor as a silicon displacement damage sensor at lower neutron and proton fluences then currently-used sensors [10];

- Correlate the silicon displacement damage sensor performance observed experimentally for proton and neutron irradiations with the calculated non-ionizing energy loss (NIEL) for three different types of silicon bipolar devices (2N1486, 2N2484, 2N2222) over a wide range of particle fluences (1-MeV(Si) neutrons: 1×10^{10} to greater than 1×10^{14}*; 4-MeV(Si) protons: 1×10^{10} to 1×10^{13}*).

The following sections will develop the fundamental theory of device physics and particle/crystal interactions necessary to understand the primary effects of displacement damage and ionizing radiation on BJTs. The methodology for using displacement damage sensors is outlined and the devices and facilities utilized for experiments are described. The measurements attainable by using the three different type bipolar devices as particle fluence sensors as well as notable observations are included in the results section. A discussion section addresses physical complexities and considerations for measuring displacement damage before the concluding remarks. Fig. 1 is the cartoon representation of a typical bipolar device cross-section and is representative of the devices used in this thesis.

---

* Units: particles of a particular energy per square centimeter, or the equivalent thereof.
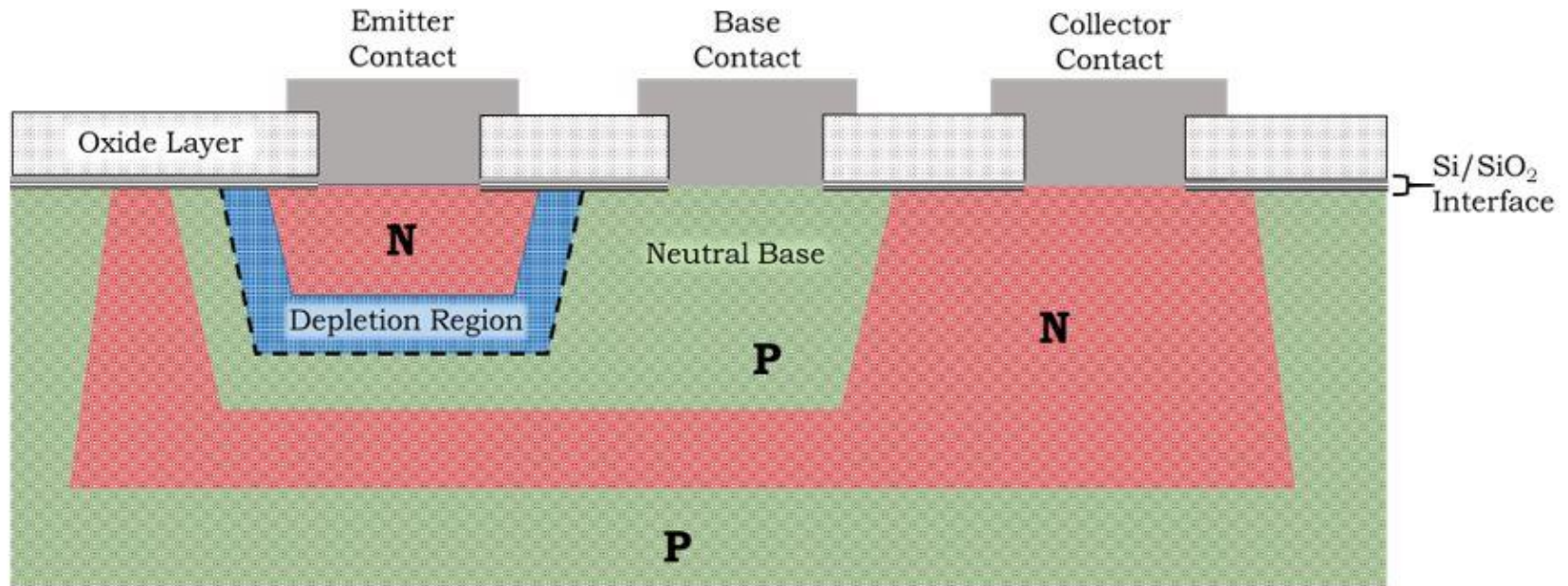
Fig. 1: Bipolar device cross-section highlighting the regions where radiation effects contribute to altering device performance. Displacement damage effects are most significant in the neutral base region and emitter-base depletion region; whereas, total ionizing dose effects appear in the oxide layer over the base and at the silicon/silicon dioxide interface.

Chapter II: Theory

This section discusses the BJT device physics and energetic particle/crystal phenomena necessary to understanding the impact of radiation induced displacement damage and ionizing radiation dose on BJT performance changes (e.g., gain degradation). Context is provided for previous research developments and the historical roots of displacement damage. Once this fundamental framework is established, an overview of the standardized displacement damage sensor methodology is presented.

Section A: Bipolar Device Physics

The BJT was invented by John Bardeen, Walter Brattain, and William Shockley in 1947 and honored with the Nobel Prize in 1956. The basic model describing current flow in a BJT is referred to as the Ebers-Moll model [18]. The BJT is a minority carrier device (because its operation depends on both majority and minority carriers) and its current gain is inherently dependent on defects that reduce minority carrier lifetimes. Defects exist in BJTs with and without energetic particle exposure because of imperfect manufacturing processes. Recombination processes associated with defects that alter current flow in the base and emitter-base depletion region are understood using the Shockley-Read-Hall model [18]. The connection between energetic particle fluence and gain degradation are described by the Messenger-Spratt equation [9].

Current and voltage can be applied and measured at the three contacts of a bipolar transistor: the collector, the base, and the emitter. The flow of electron current from emitter to collector in an NPN transistor operated in forward-active mode can be summarized as follows: Electrons are injected from the forward-biased emitter-base junction, diffuse across the neutral base, and are swept through the base-collector depletion region by the electric field [18]. The current components that are seen at the
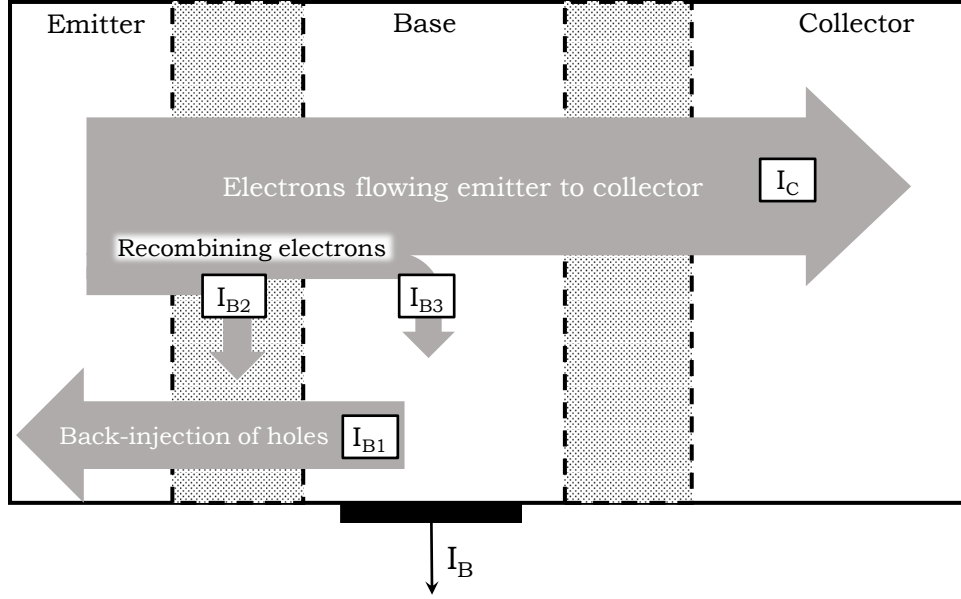
Fig. 2: Primary current components in forward-active biased npn bipolar transistor. Recombination processes associated with I_{B2} and I_{B3} increase with the addition of energetic particle induced displacement damage.

base contact (base current) include the back-injection of holes from the base to the emitter, recombination current in the emitter-base depletion region, and recombination current in the neutral base. Fig. 2 shows the current components for a forward-biased NPN transistor. The following current equations can be understood by considering the modulation of barrier height by applied voltage, visualized in the energy band diagram in Fig. 3. A pristine device without significant defect concentrations will have the base current dominated by the back-injection of holes. In normal operation, collector and base current can be represented as I_C and I_{B1} in the eqs. 2 and 3. Both ideal current components follow that ~60 mV being applied across the emitter-base junction results in a decade of increased current (eq. 4).

$$I_c = A_e \frac{q D_{nB} n_i{}^2}{N_B W_B} \exp\left(\frac{q V_{BE}}{kT}\right) \tag{2}$$

$$I_{B1} = A_e \frac{q D_{pE} n_i{}^2}{N_E L_{pE}} \exp\left(\frac{q V_{BE}}{kT}\right) \tag{3}$$

$$\ln(I_C \text{ or } I_{B1}) \propto \left(\frac{q}{kT}\right) V_{BE} \tag{4}$$

where I_C is the collector current, I_{B1} is the base current due to back injection of holes, A_e is the emitter-base junction area, $\frac{q}{kT}$ is the thermal voltage, D_{nB} is the diffusivity of electrons in the base region, n_i is the carrier concentration in the base, N_B is the base doping concentration, and W_B is the width of the neutral base region. D_{pE} and N_E are the corresponding values in the emitter region while L_{pE} is the diffusivity of holes in the emitter. Eq. 4 is in the log-lin form BJT current and voltage are typically plotted in.

In addition to back-injection of holes into the emitter, base current has two contributions from recombination that depend on the minority carrier lifetime, which
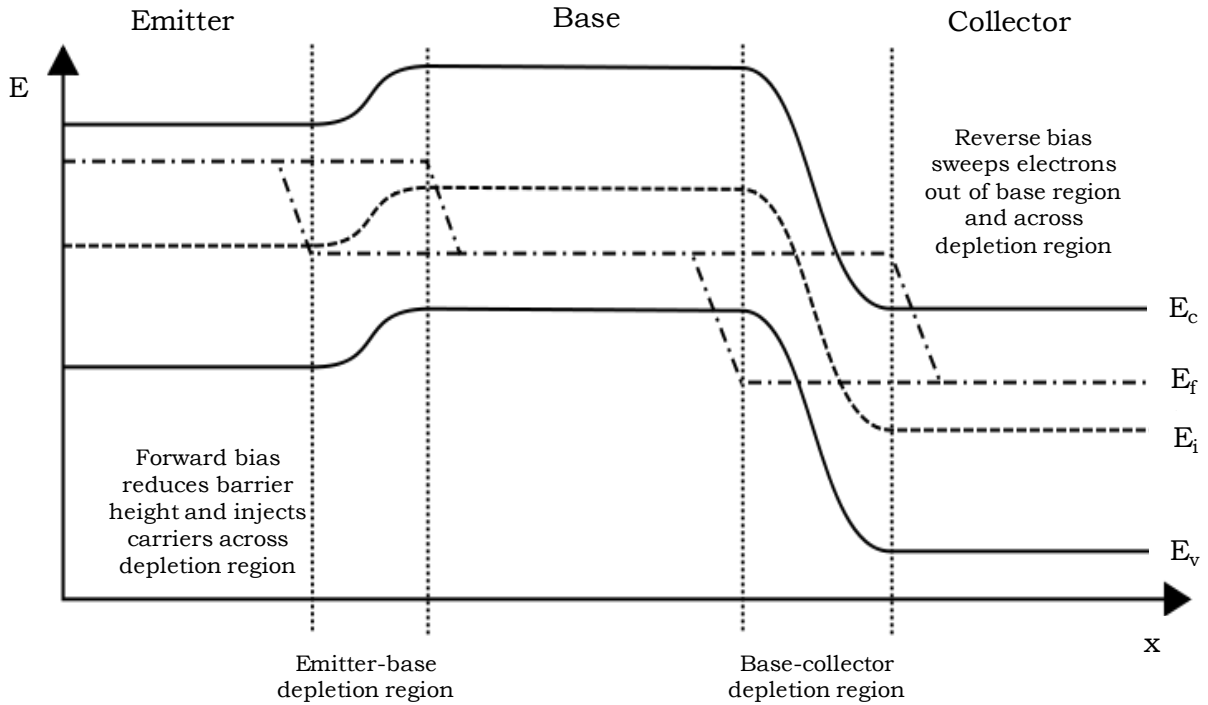
Fig. 3: Energy band diagram of a forward-active biased npn bipolar transistor. At each junction the applied bias creates a quasi-fermi level for both electrons and holes whose distance from the respective band edge modulates that charge carrier's concentration. The curvature of an energy band indicates the presence of an electric field that can act on charge carriers (e.g. $\varepsilon = \frac{1}{q}({dE_c}/{dx})$).

9

represents the average amount of time carriers exist before recombining. Minority carrier lifetime is dependent on the accessibility of defects that act at recombination sites. The lifetime decreases as the probability of encountering a defect and recombining is increased.

Recombination current originating in the emitter-base depletion region has an ideality factor ('n' in $exp\left(\frac{qV_{BE}}{nkT}\right)$) of approximately 2, while recombination current occurring in the neutral base has an ideality factor of approximately 1 [19] (see Table I). Recombination in the emitter-base depletion region can occur at the Si/SiO$_2$ interface and be proportional to surface recombination velocity or it can occur in the material bulk and be proportional to the minority carrier lifetime [20]. Due to the large ideality factor (n $\cong$ 2) associated with emitter-base depletion region recombination, its effect is more prevalent at low-bias conditions. The difference in ideality factors can be related to the availability of charge carriers in each region. In the depletion region the presence of both carrier concentrations is exponentially dependent on the applied bias. In contrast, in the bulk region there is an abundance of majority carriers and only the minority carrier concentration is limited by the applied bias.

The equations in Table I provide insight into the subthreshold slope expected from each recombination current contributor. Shockley-Read-Hall (SRH) recombination theory can provide a better understanding of how defect concentrations (that will later

Table I: Recombination current contributions from different regions in a bipolar junction device.

Emitter-base depletion region	Neutral base
$\ln(I_{B2}) \propto \left(\frac{q}{2kT}\right) V_{BE}$	$\ln(I_{B3}) \propto \left(\frac{q}{kT}\right) V_{BE}$
[~120 mV/decade]	[~60 mV/decade]

be linked to energetic particle irradiation) contribute to changes in device performance by increasing base current. The SRH representation for recombination rate in both regions of interest (the emitter-base depletion region and the neutral base) can be approximated as [18]:

$$U = \frac{(pn - n_i^2)}{\left[p + n + 2n_i cosh\left(\frac{E_t - E_i}{kT}\right)\right]\tau_0}$$

(5)

Where U is the recombination/generation rate, p and n are the carrier concentrations, E_i is the intrinsic energy level, E_t is the trap energy level, and τ_0 is the carrier lifetime (with the assumption that electron and hole recombination cross-sections are equal). If the pn product is greater than the intrinsic carrier concentration squared, n_i^2, then U will be positive and there will be net recombination. If U is negative there will be net generation. The denominator at a minimum when $E_t = E_i$, therefore U is at a maximum when the trap energy level is close to the middle of the bandgap (midgap). This is depicted in Fig. 4 where the bold line represents recombination in an un-depleted region
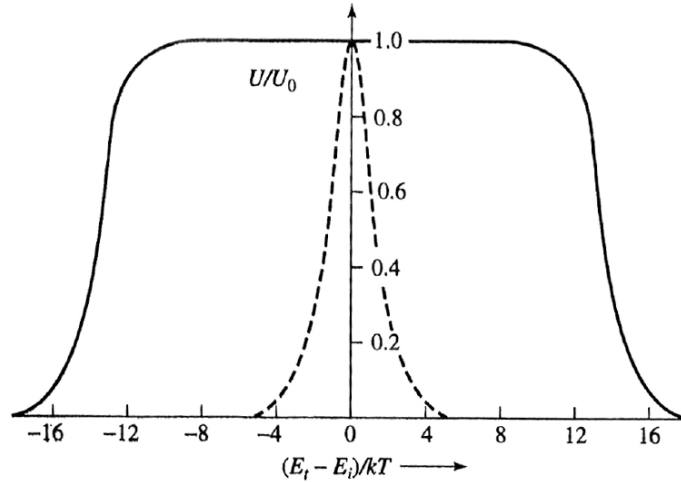
Fig. 4: Shockley-Read-Hall recombination/generation rates as a function of trap energy level with respect to the intrinsic level. The bold line represents net recombination in an un-depleted region and the dashed line represents generation in a depleted region [18].

11

and the dashed line represents generation in in a depleted region [18]. Recombination in a depleted region is maximized by two conditions: a trap energy level near midgap as well as recombination events occurring at a location within the depletion region where the hole concentration and electron concentration are approximately equal (n=p). Most important for this work in eq. 5, is that the recombination rate increases with decreasing carrier lifetime, τ_0. Minority carrier lifetime and transistor current gain are typically proportional, with current gain defined as the ratio of collector current to base current.

The principle displacement damage effect of particle radiation on bipolar device performance is an increase in the amount of defects with trap energy levels within the forbidden bandgap that take part in SRH recombination processes, increasing the base current components I_{B2} and I_{B3} and decreasing the current gain. In Fig. 5, an example Gummel plot (log I_C and I_B vs. V_{BE}) is shown for a 2N1486 device used in this work.
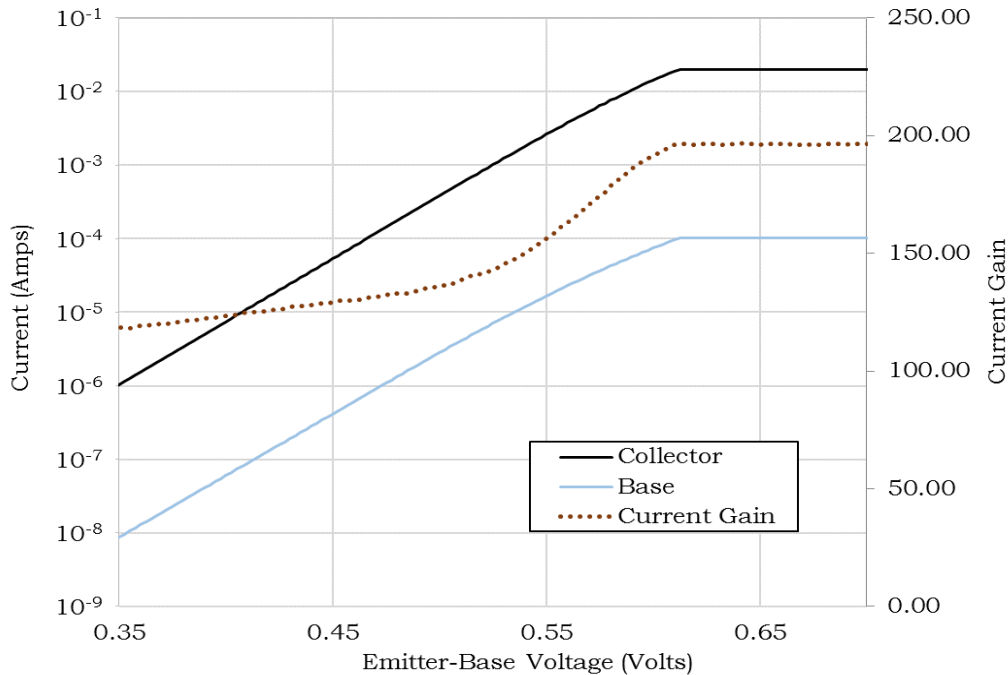
Fig. 5. An example Gummel plot with log(I_c) and log(I_b) plotted vs. emitter-base voltage. Plotted on the secondary axis is the corresponding current gain. A compliance current of 20 mA in the collector is reached by ~0.6 V.

Section B: Displacement Damage

As an energetic particle traverses the crystalline lattice of a solid it can transfer its energy to the atoms that make up the host lattice through ionizing and non-ionizing processes. In ionizing energy transfer processes, the incident particles transfer their energy to electrons by promoting them from the valance band to the conduction band of the lattice atoms (i.e. the creation of electron-hole pairs) [21]. In non-ionizing processes, energetic particles collide with and displace lattice atoms (i.e. displacement damage) [22]. The non-ionizing processes that occur with proton and neutron irradiation include elastic scattering, where the kinetic energy of the incident particle and the target atom are conserved, and inelastic scattering, where a portion of the kinetic energy is transferred to other processes. Other processes transfer energy to phonons, nuclear excitation, or nuclear reactions such as (n,p) and (n,α) reactions [22]. Rutherford (coulombic) scattering will also occur between the charge bearing protons and lattice atoms [20] [23]. The lattice atom that is initially displaced is referred to as the primary knock-on atom (PKA).

The significance of understanding how energetic particle radiation can alter the properties of a material was first highlighted by Eugene Wigner in 1946 when presenting experimental details of the first nuclear reactor experiments, one year before the invention of the transistor [23]. The early studies of displacement damage effects in materials, especially material embrittlement, are summarized by Kinchin and Pease [24].

The first study of displacement damage effects on semiconducting materials (Germanium in this case) was produced one year after the invention of the transistor in 1948 by Davis et. al [25]. In semiconducting materials, the study of displacement

damage is especially interesting because the resulting defects can substantially alter the properties of the material by creating localized defect states in the otherwise forbidden bandgap. The dominant effect of localized states in the bandgap is to act as electron-hole recombination centers. In 1958, Messenger and Spratt produced that equation that has been successful in describing an enduring relationship observed between particle fluence and device performance, measured as current gain degradation or equivalently as increases in base current [9]. A cartoon depiction of displacement damage can be seen in Fig. 6.

The Messenger-Spratt equation presented in Chapter I (eq. 1) describes the fundamental observed effect of displacement damage in bipolar devices, the reduction of minority carrier lifetime. The minority carrier lifetime decrease ($\Delta\tau$), that occurs with the introduction of recombination centers, is directly related to the increase in base current in the bulk region by eq. 7 and the emitter-base depletion region eq. 8, analogous to the relationships presented in Table I [26].
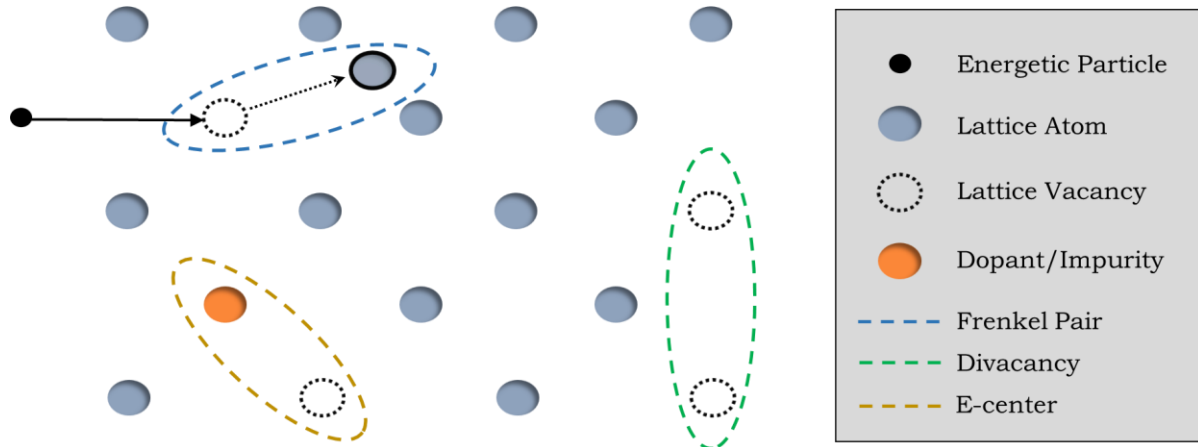
Fig. 6: Defects in a crystalline solid. In the upper left, an energetic particle dislodges a PKA that becomes an interstitial. Pairs of interstitial atoms and vacancies are known as Frenkel pairs and are the most common defect created with energetic particle bombardment. E-center defects (impurity/vacancy pairs) and divacancies are less mobile than Frenkel pairs and substantially anneal only at elevated temperatures. These defects also have energy levels near midgap, increasing their recombination efficiency.

$$\Delta I_{B2} = qA_e W_D \frac{n_i}{2\Delta\tau} exp\left(\frac{qV_{BE}}{2kT}\right)$$

(6)

$$\Delta I_{B3} = qA_e W_B \frac{n_i^2}{2\Delta\tau N_B} exp\left(\frac{qV_{BE}}{kT}\right)$$

(7)

The change in the minority carrier lifetime encapsulates the effect induced by the displacement of lattice atoms and the creation of recombination centers, which is a complex process. Bombarding particles can displace atoms in the host lattice if they have energy above the material specific displacement threshold energy, T_d (for silicon, T_d = ~ 21 eV [27]). In the case of low to moderate energy electrons [28] and low energy protons and neutrons point defects are created (i.e. individual vacancy-interstitial pairs, or "Frenkel pairs") [22]. The interstitial (I) atom and the single vacancy (V) from the initial Frenkel pairs are both very mobile and can readily recombine (anneal). However, if a vacancy migrates into close proximity of another vacancy or to a dopant impurity atom, a more stable and less mobile defect can form. Stable defects made from two vacancies are referred to as a divacancy (V_2) and a vacancy and an impurity combination is referred to as an E-center (e.g. vacancy-phosphorus [VP]) (see Fig. 6) [22] [29]. The ability for defects to migrate and their dependence on time and temperature creates the first complication.

Table II: Silicon defect types and positions in the forbidden bandgap [56].

Defect	E_T [eV]	Cross section [cm^2]
V	E_v+ 0.47	σ_p = 9·10^{-16}
I	E_c − 0.44	σ_n = 2·10^{-15}
VP	E_c − 0.46	σ_n = 4·10$^{-15.}$
V_2	E_c − 0.43	σ_n = 2·10^{-15}

Representative energy levels which these defects can introduce in the forbidden bandgap are shown in Table II. The energy level of each trap affects its efficiency in capturing electrons/holes and varies depending on the type of defect, a second

15

complication. Trap energies near midgap display the largest electron and hole capture cross-sections, making them effective as recombination sites where either an electron or a hole is captured. The divacancy and E-center defects are only capable of substantial time-temperature annealing at temperatures of approximately 420 K or higher [22].

With higher energy particles, enough energy can be transferred to the lattice atoms that, after their initial displacement, dislodged atoms will collide and displace additional lattice atoms in a cascade. The resulting creation of many displaced atoms is referred to as a cascade and may contain densely clustered defects. The initially displaced recoil particle is the PKA. For particle elastic and inelastic scattering, this PKA is one of the lattice atoms. For a neutron transmutation reaction, such as a (n,p) or (n,α) reaction, this PKA atom will have a different atomic number and atomic weight. The complexities presented by defect cluster formation and variable defect types are best addressed with computational modeling and are areas of active research [29] [30]. The impact of these complications will be discussed in Chapter VI; however, the Messenger-Spratt equation for the devices and environments in this thesis still applies.

A simplified expression for approximating only the amount of elastic and inelastic interactions that contribute to displacement damage for a given particle and energy is referred to as non-ionizing energy loss (NIEL, 's') [14] [22]:

$$NIEL = \left(\frac{N}{A}\right)[\sigma_e T_e + \sigma_i T_i] \tag{8}$$

where N is Avogadro's number, A is atomic weight, σ_e is the elastic interaction cross-section, σ_i is the inelastic interaction cross-section, T_e is effective average recoil energy from elastic interaction, and T_i is the effective average recoil energy from inelastic interaction. NIEL provides a good way to approximate how different particles and

energies will create displacement damage and has been used with significant success [14] [31]. NIEL does have limitations and does not address the complete physical reality; complications that arise when applying NIEL for displacement damage correlations are addressed in Chapter VI. Fig. 8 shows how NIEL can provide effective particle/energy damage correlation for protons and neutrons. The damage factor along the y-axis in Fig. 7 comes from the Messenger-Spratt equation and its calculation is presented in Section D of this chapter.
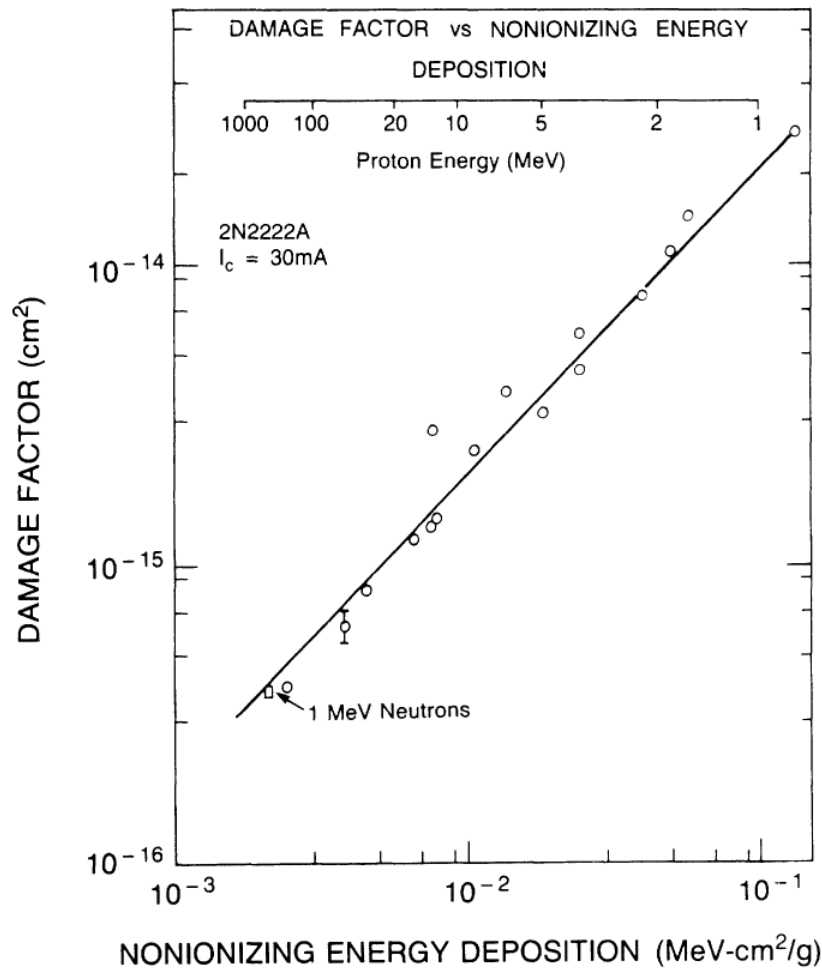
Fig. 7: Non-ionizing energy deposition vs. damage factor for 1-MeV(Si) equivalent neutrons and a range of proton energies. The value of NIEL is shown to correspond directly with the damage factor in the Messenger-Spratt equation [10].

17

Section C: Ionizing Radiation Dose

Ionizing energy deposition can occur when an energetic ion, photon, or electron passes through a material. The resulting electron-hole pairs can contribute to the degradation of bipolar devices by reducing current gain and increasing base current [21] [32] [33] [34]. During irradiation, ionizing dose generates transient photocurrents measurable at all gates that can disrupt device measurements [11] [31]. After irradiation, base current increases due to two total ionizing dose (TID) effects: the creation of interface traps and trapped charge in the oxide [21] [32].

Oxide- and interface traps occur at oxygen vacancies in SiO_2 and dangling silicon bonds at the silicon/silicon dioxide interface [21]. Proton transport to the interface creates the dangling silicon bonds (P_b centers) as well as gaseous hydrogen (Fig. 8, right). Interface traps, occurring as P_b centers, act as recombination sites. Recombination sites at the interface contribute to increasing the surface recombination velocity [35]. Surface recombination occurring near the emitter-base depletion region will increase base current and have an ideality factor of 2, much like with displacement damage. Oxide trapped charge near the emitter-base junction alters the surface electric potential and
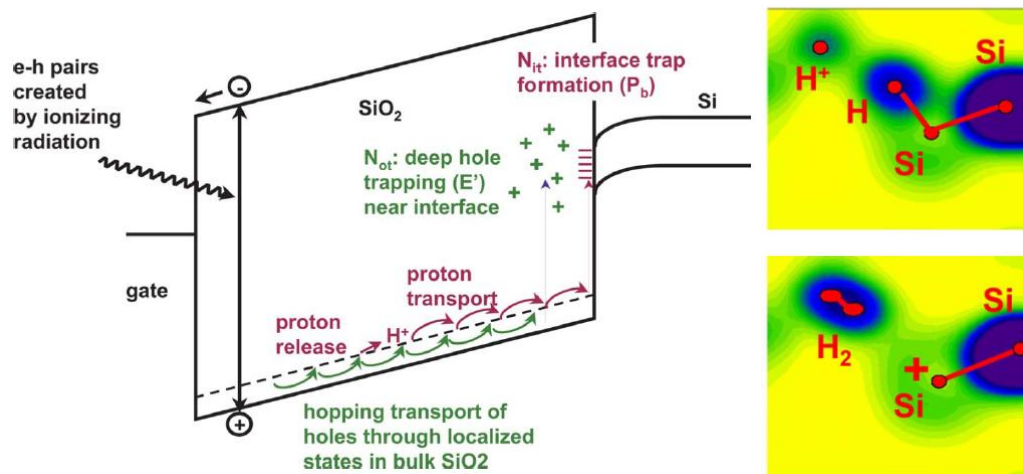
Fig. 8: Ionizing dose effects (left) [34] and creation of Si-dangling bonds (right) [21].

modulates the size of the emitter-base depletion region [32] [35]. In Fig. 8 is a depiction of TID effects.

TID effects vary with ionizing radiation sources. Different types of radiation can result in different initial separation distances (thermalization distance) between electrons and holes [36]. Different charge carrier density distributions will recombine, migrate, and/or form interface and oxide traps at different rates. In some circumstances, degradation increases with lower ionizing dose rates, a phenomenon known as Enhanced Low Dose Rate Sensitivity (ELDRS) [37]. The fraction of charge carriers that survive initial recombination is referred to as charge yield [38]. Charge yield can be related to the mass-stopping power of different radiations. Fig. 9 show the mass-
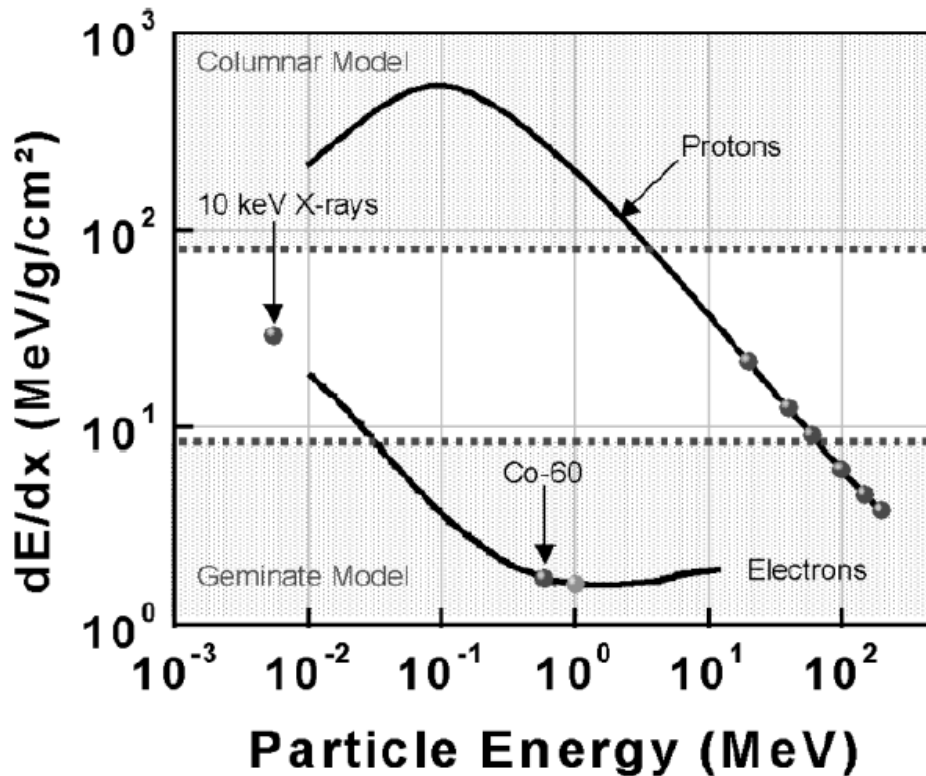
Fig. 9: Stopping power of various ionizing radiation sources. The secondary electrons from 10-keV x-rays have a stopping power approximately equal to 20-MeV protons. The secondary electron stopping power from Co-60 gamma rays are also labeled [48].

stopping power for protons of different energies and the secondary electrons from 10 keV x-rays, and cobalt-60 gamma rays. Important in Fig. 9 is the approximately equivalent mass-stopping power for 10-keV x-rays and 20-MeV protons. The ionization charge yield behavior for various protons, x-rays and gamma rays is shown in Fig. 10. When the separation of individual electron-hole pairs is large compared to the thermalization distance, a geminate (consisting of identical pairs) model is applicable which treats them as specific, individual pairs [36]. If the separation of different pairs is similar or less than the thermalization distance, the entire yield of charge carriers must be treated statistically with a columnar model (Fig. 10) [36]. TID effects are also dependent on applied bias conditions and dose rate, however these factors are not within the scope of this work.
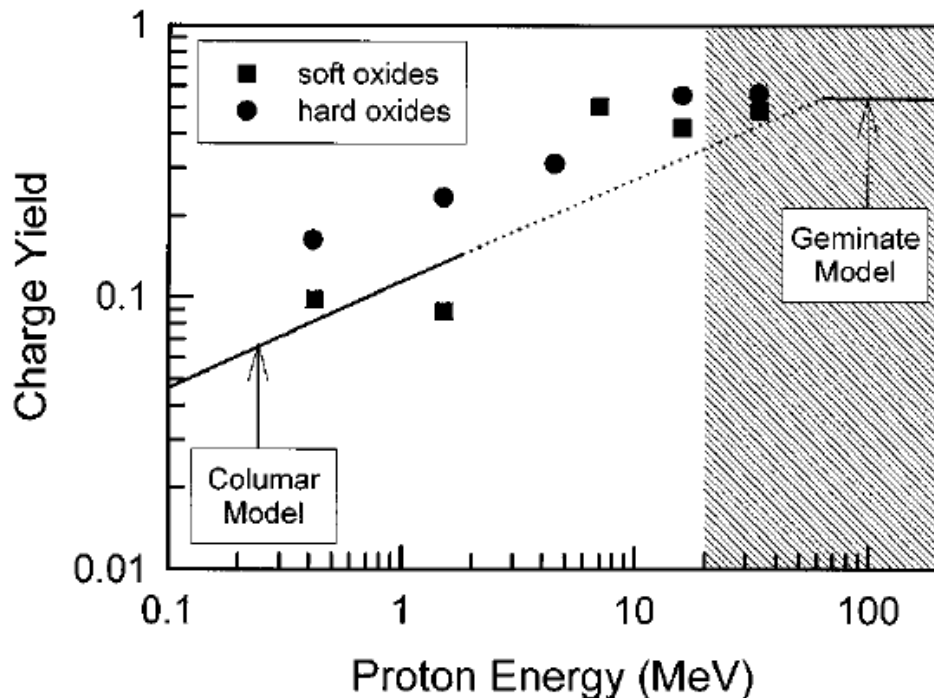
Fig. 10: Charge yield ratio for a range of proton energies [36]. The geminate model applied when electron-hole pairs generated by ionization are separated further apart than the mean separation between pairs. Whereas a columar model is used when electron-hole separation is less than the the mean separation between different pairs.

20

Section D: Standard Procedure for Displacement Damage Sensors

The experimental methods used in this thesis are guided by the ASTM standard test method E1855 [5]. A flow chart summarizing ASTM E1855 can be seen in Fig 11. The test method provides instructions for the use of 2N2222 silicon transistors as displacement damage sensors; however, its methodology can be extended to 2N1486 and 2N2484 silicon transistors.

The procedure begins with measuring each transistor's current gain at a reference value of 1 mA of collector current. This reference value remains consistent throughout the procedure and was verified to be applicable to the 2N1486 and 2N2484. The reference is appropriate because it is in the linear region for forward-active bias, no injection current annealing has been observed experimentally, and it is convenient for standardized procedure [10]. A common-emitter circuit scheme is used during readout (Fig. 12).
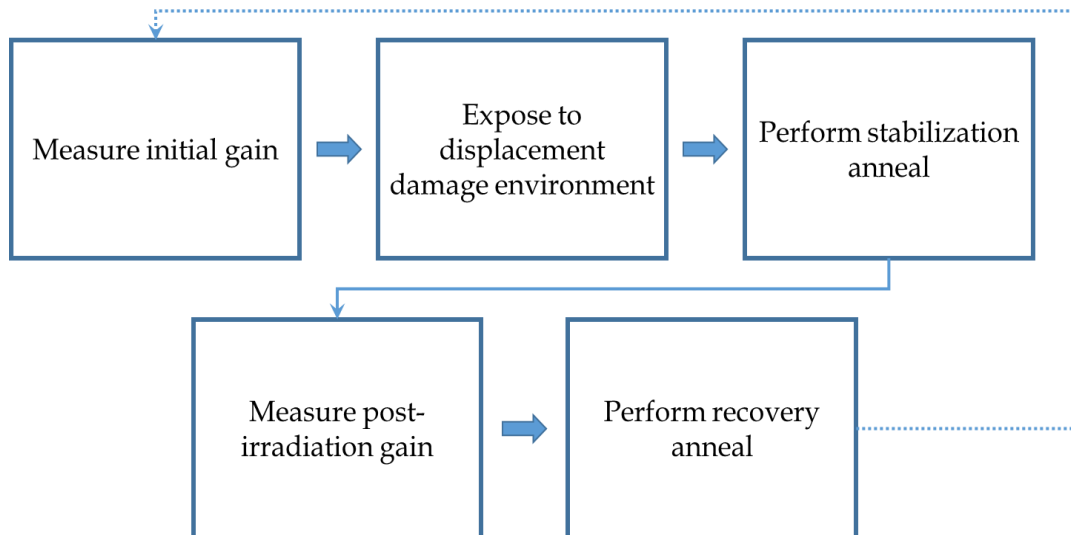
Fig. 11. Flow chart summarizing the displacement damage sensor procedure. After the recovery anneal is performed the procedure can be repeated. During each step of the procedure, besides IV measurements, the device is unbiased with leads grounded. Note: Before measuring the post irradiation gain the transistor is exposed to a thermal stabilization anneal of 80° C for 2 hours [10].
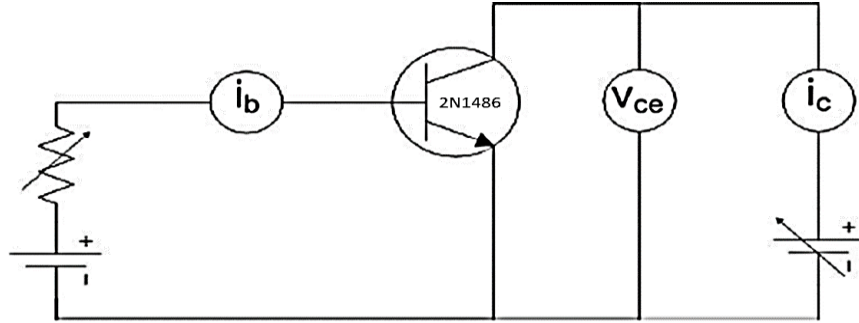
Fig 12. Common-emitter circuit diagram used to measure current gain.

Once the initial current gain values are recorded, a calibration exposure is performed in a reference neutron environment. The reference environment must be well-characterized and monitor dosimetry must be included to enable the determination of the reference 1-MeV(Si) equivalent fluence. To be considered well-characterized, the neutron radiation field must be stable, reproducible, and a record must be available for the spatial and energy-dependent radiation intensity during irradiations. This data must then be incorporated with nuclear reactor physics and radiation transport models to create a detailed understanding of the radiation environment impingent upon the DUT.

After the devices are exposed in the calibration environment, they undergo a two-hour elevated temperature "stabilization" anneal at ~350 K. The stabilization anneal is used to reduce the amount of gain readout variability due to time-dependent annealing that occurs at room temperature. The stabilization anneal is particularly helpful since it is not always convenient to fix the exact time after the irradiation at which the transistor current gain is measured as well as to control the environmental temperature during this time interval. The stabilization anneal is intended to eliminate sensitivity to normal variations in the storage temperature of the device during a potential several day delay between exposure and gain measurement. After the stabilization anneal, a post irradiation gain measurement is taken (β_{post}).

With a change in current gain and reference 1-MeV(Si) equivalent fluence known, the displacement damage factor (DDF) for each individual device can be calculated by rearranging eq. 1 into eq. 10. The DDF incorporates the damage factor and transistor cut-off frequency.

$$\text{DDF} = \frac{K_1}{f_T} = \left(\frac{1}{\beta_{post}} - \frac{1}{\beta_0}\right)\Big/\Phi_{1-\text{MeV(Si)}} \tag{9}$$

Once the DDF for each transistor is known, the devices can be used in the determination of 1-MeV(Si) equivalent fluences in unknown environments by following eq 11.

$$\Phi_{1-\text{MeV(Si)}} = \left(\frac{1}{\beta_{post}} - \frac{1}{\beta_0^*}\right)\Big/DDF \tag{10}$$

The new initial current gain measurement (β_0^*) in eq. 11 is performed after an elevated time-temperature anneal of 24 hours at ~450 K before for the next irradiation (see Fig. 11) [5]. This is referred to as the "recovery" anneal with the intention of annealing some of the damage and restoring the device sensitivity. The ASTM annealing conditions are further investigated in Chapter IV.

The current standard requires the use of control transistors to provide a relative temperature correction. This enables practical application of the standard for a broad group of users and experimental circumstances. Experiments at SNL did not require the use of control transistors because all readouts were performed with the device temperature controlled. At Vanderbilt University all measurements and experiments were performed in the same climate-controlled laboratory basement, which introduces negligible change in current gain readout (± 2 K → ± 1%, see Fig. 13).

Chapter III: Experiment Details

The radiation exposure experiments for this thesis were performed at Sandia National Laboratories located in Albuquerque, New Mexico and Vanderbilt University (VU) located in Nashville, TN. Sandia National Laboratories (SNL) is a Department of Energy laboratory. SNL is home to many radiation producing facilities including: Ion Beam facility, Z-Machine, Hermes-III, Saturn, Annular Core Research Reactor (ACRR), and the Gamma Irradiation Facility (GIF) [39]. VU is home to the largest university based radiation effects research institute, the Institute for Space and Defense Electronics (ISDE) and the Radiation Effects and Reliability research group. VU has experimental capabilities with radioactive sources, ARACOR x-ray irradiators, and a pelletron particle accelerator [40]. In this work the ACRR [41] and GIF at SNL are utilized as well as the ARACOR and pelletron at VU.

The displacement damage and ionizing dose experiments were performed on three different types of bipolar transistors, all of the NPN polarity. The devices are all commercial off-the-shelf (COTS) produced by Microsemi Corporation and have the identification numbers: 2N1486, 2N2222, and 2N2484. The 2N1486 and 2N2484 were chosen for their low cut-off frequency parameters, which indicates the potential for increased sensitivity to displacement damage. The 2N2222 was selected for its long track record of use in radiation effects research [3] [13] [14] [31] [42] [43] and the ASTM E1855 standard test method, which is based upon the 2N2222. Each of these parts appear in the NASA radiation shielding report for the International Ultraviolet Explorer with measurements suggesting their level of sensitivity [44]. The following sections describe the characterization of these parts and the description of each test environment.

Section A: Devices and I-V Measurements

The current and voltage (I-V) characteristics of each device are taken as Gummel plots acquired with either a Hewlett Packard 4142B parameter analyzer with an HP 16058A Test Fixture (used at SNL) or Hewlett Packard 4156A parameter analyzer and a custom fabricated prototype board (used at VU).

For the SNL experiments, the devices were measured a significant duration after irradiation due to neutron activation and decay processes. Devices were mounted in a custom-sized temperature-controlled mounting block installed inside the test fixture. During readout, the mounting block is maintained at precisely 273 K using a Lakeshore temperature controller. A one-minute delay was allowed for each transistor to equilibrate in temperature with the mounting block and gloves were worn to reduce the amount of body heat absorbed by the device from the experimenter. Experimental measurements with variable device temperature indicated a dependence of the gain measurement on temperature of less than +0.5% per Kelvin (Fig. 13). Due to the weak dependence of current gain on device temperature and the relatively constant temperature maintained in the radiation effects laboratory at VU, the temperature control block was determined to be unnecessary for the VU experiments (see Fig. 13).

The parameter analyzer was setup to obtain a Gummel plot with the following parameters:

- The collector voltage is set at a constant 10 V
- The emitter voltage is held common, 0 V
- The base voltage is varied in sweep mode from 0 to 0.75 V
- A compliance current of 20 mA is set for the collector current

Example Gummel plots obtained for each device before and after irradiation are shown in Figs. 15 and 16. The base current and current gain are shown after

considerable degradation (50%-75%). At emitter-base bias below ~0.3 volts, the base current is below the effective measurement range of the parameter analyzers and a noisy, un-physical current gain is recorded; for this reason, the plots begin at an emitter-base bias of 0.35 volts. The base current ideality in each device is shown to increase (decreased slope), indicating increased emitter-base depletion region recombination. Current gain measurement distributions for 2N1486 transistors before and after irradiations are shown in Fig. 17 and appear Gaussian, although limited by sample population.

Scanning electron microscope images of the 2N2222 and 2N1486 can be seen in Fig. 14. The increased fluence sensitivity of the 2N1486 to displacement damage is due to its larger base width (~37 µm vs. ~9 µm). The square of base width is inversely proportional to cut-off frequency; therefore, base width is also an indicator for inherent high sensitivity to displacement damage [45].
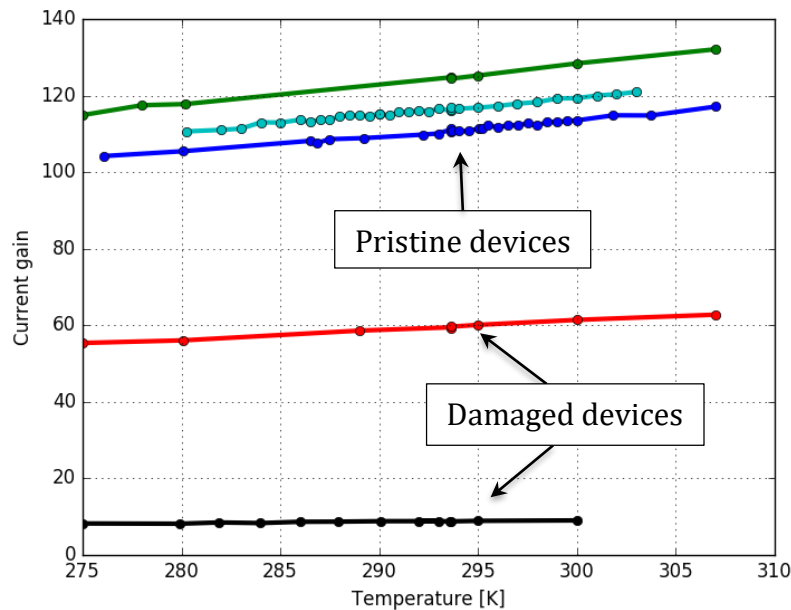
Fig. 13 Temperature dependence of current gain measurements. Measurements are performed on three control transistors, one moderately damaged, and one heavily damaged device. All transistors depicted are 2N1486.

26
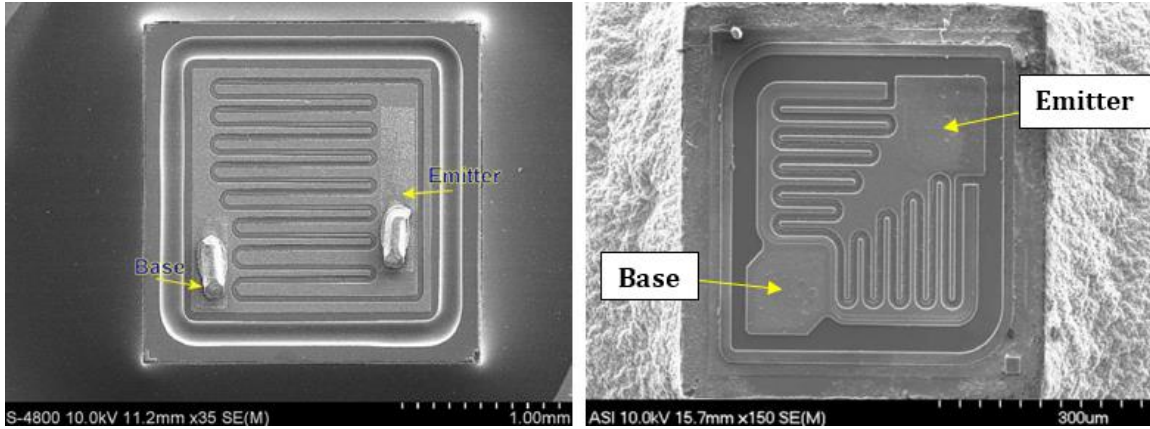
Fig. 14: Scanning electron microscope images of the 2N1486 (left) and 2N2222 (right). The feature sizes of each look similar however they are taken at different degrees of magnification, 1.00 mm for the 2N1486 vs. 300 μm for the 2N2222.
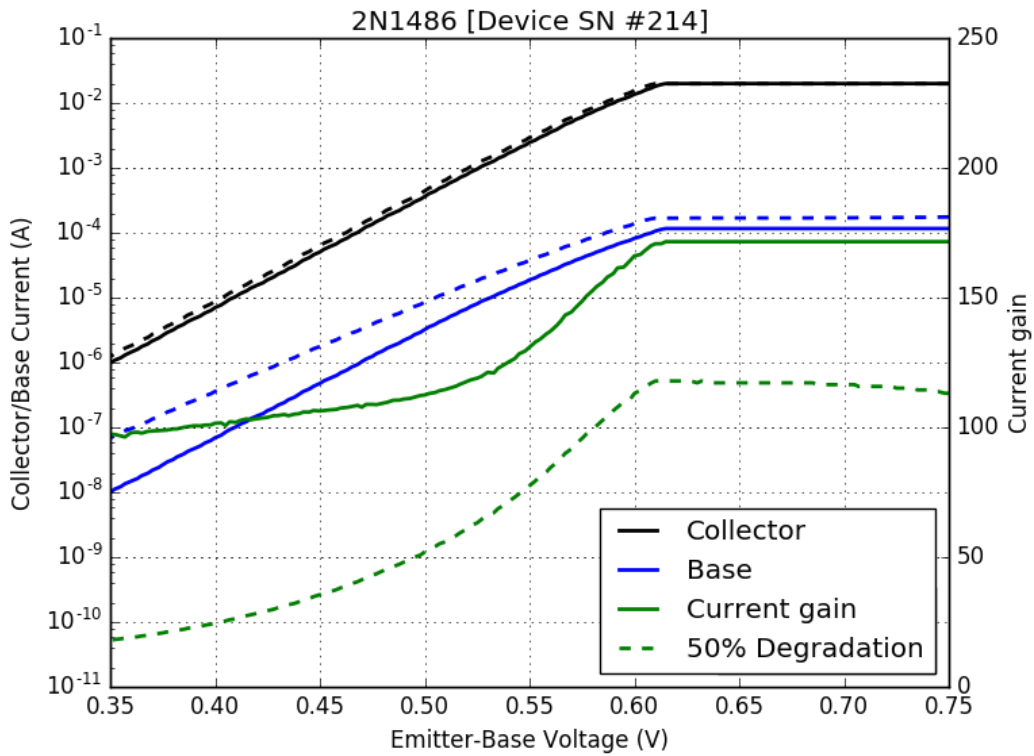
Fig. 15: Gummel plot and current gain of pristine 2N1486 and after significant damage resulting in 50% current gain degradation.

27
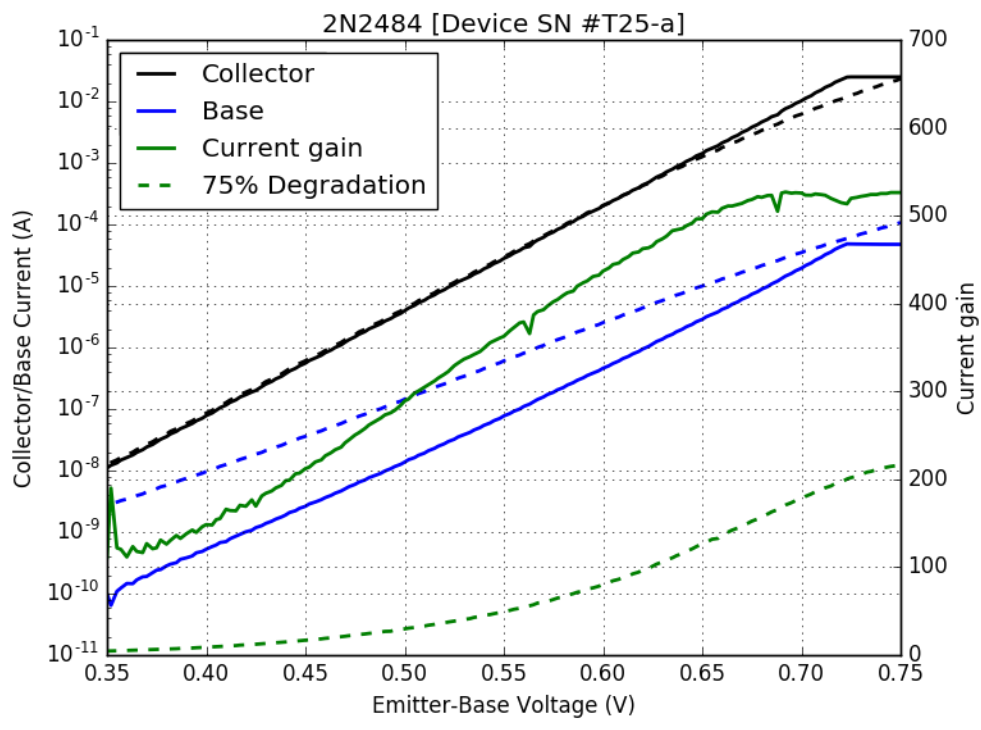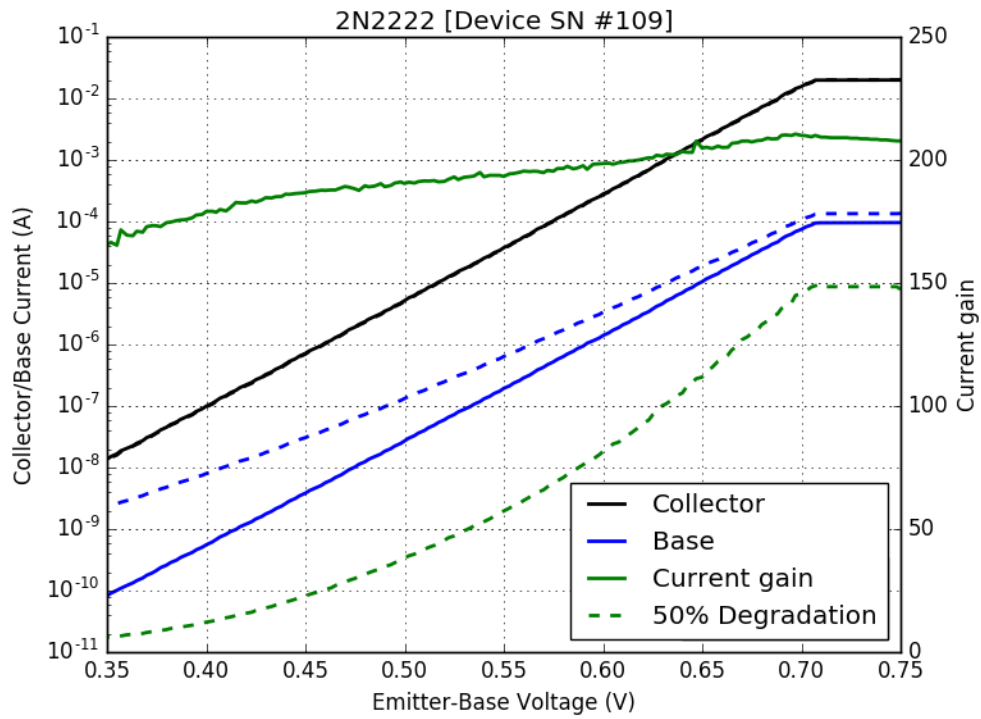
Fig. 16: Gummel plot and current gain of pristine 2N2222 and after significant damage resulting in 50% current gain degradation (upper) and 2N2484 (lower) with 75% current gain degradation.
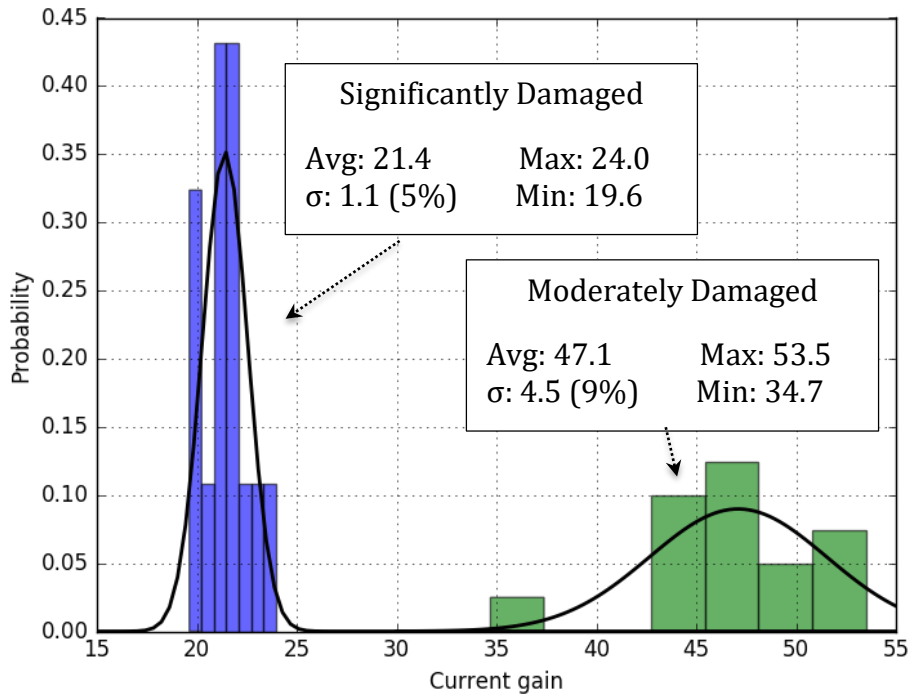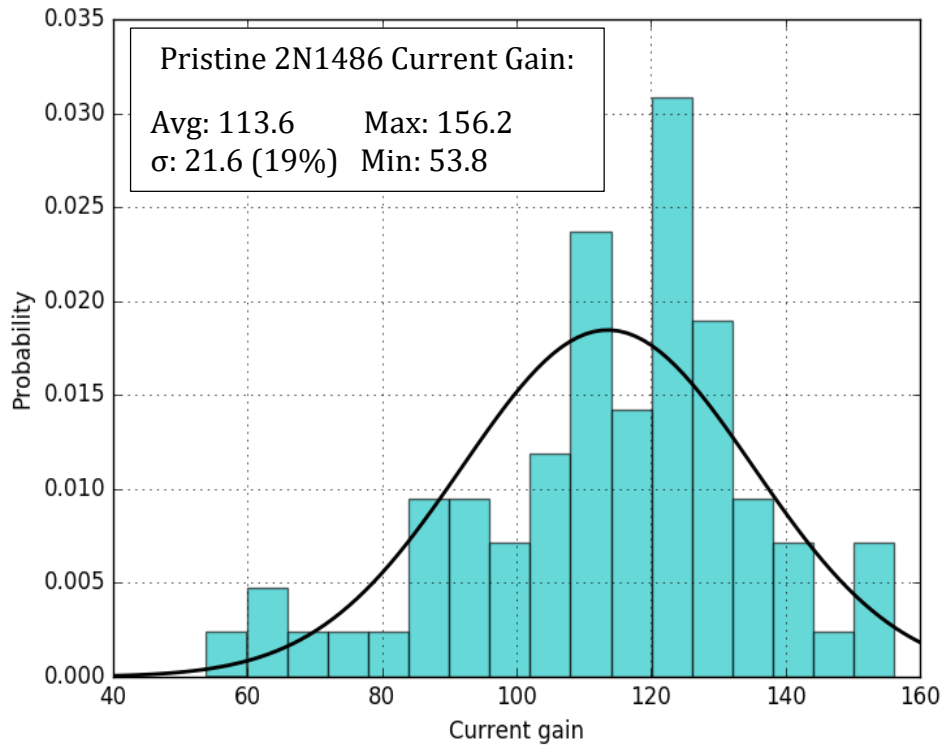
Fig. 17: Current gain measurement distributions at the reference point (Ic = 1 mA) for 70 pristine 2N1486 transistors (upper) and two levels of current gain degradation in two groups of 15 transistors (lower). The current gain measurements appear representatitive of a normal distribution (Gaussian) considering the small sample size. Standard deviation is shown to decrease with severity of degradation.

Section B: Radiation Environment Descriptions

The Annular Core Research Reactor and Gamma Irradiation Facility are located in Technical Area V of SNL in Albuquerque, New Mexico. ACRR is a pool-type research reactor that can operate in a pulsed or steady-state mode. ACRR features a large, dry central cavity and epithermal/fast neutron energy spectrum originating from fission in uranium dioxide/beryllium oxide fuel [41]. Fission results in the release of significant gamma and neutron radiation.

In ACRR, the epithermal/fast flux can be tailored using different spectrum modifying bucket configurations. To generate a spectrum of high energy neutrons that participate in displacement damage, as well as minimize ionizing dose from gamma radiation, the lead-boron bucket (LB-44) configuration is used (spectrum in Fig. 18, bucket schematic in Fig. 20). Boron has a high thermal neutron capture cross-section
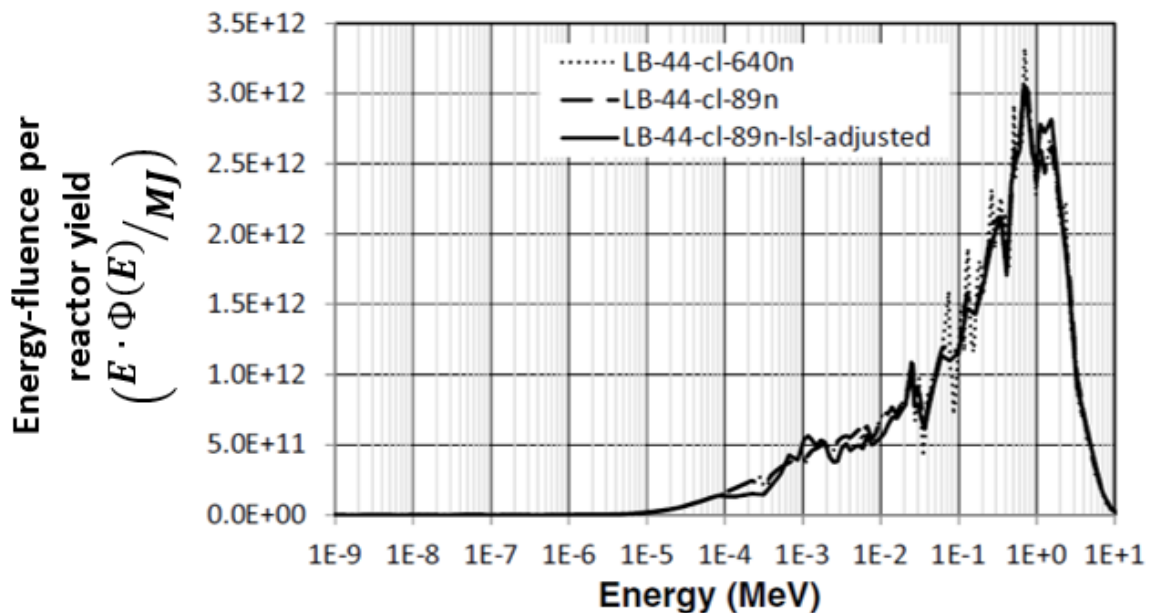
Fig. 18: Lead-boron bucket neutron energy-fluence vs. neutron energy. The neutron energy spectrum has a high energy peak with a minimized thermal neutron fluence [49]. The spectrum structure corresponds to actual reactor material neutron cross-section resonances.

and acts as a neutron poison, preventing low energy neutrons from passing through. Lead has a high atomic number which allows it's many electrons to efficiently absorb gamma radiation. The ACRR is an intrinsically safe research reactor. It features a negative temperature feedback coefficient that limits any super-critical excursions from reaching dangerous power levels.

ACRR is characterized for use as a reference neutron radiation field. Periodically, each test environment is fully characterized following standardized procedures with numerous activation foils, flux maps, and repeatability tests [6] [46] [47] [48]. During each irradiation, accompanying dosimetry is included in close proximity to the device under test (DUT). The exposure monitor dosimetry most commonly includes sulfur and nickel activation samples for fast neutron sensitivity and thermoluminescent dosimeters as an ionizing dose monitor. Sulfur is more sensitive than nickel to the high energy (>3 MeV) neutron fluence and is favored for low-fluence experiments [47].

To use a measured sulfur or nickel activation reading to infer a reference 1-MeV(Si) equivalent fluence the following equations are used with conversions provided from the latest lead-boron bucket spectral characterization report [49]. The sulfur activation reading uses a transfer calibration from a NIST californium-252 source for an equivalent fluence that must be converted to total fluence for ACRR and then to the 1-MeV(Si) equivalent fluence (eq 12). Nickel activation (via the ^{58}Ni(n,p)^{58}Co reaction) is reported in bequerels (decays per second) and follows a similar conversion (eq 13).

$$\phi_{1-MeV(Si)} = (Cf\ Equivalent)\ x\ 4.837\ (\pm 4.74\%) \frac{Total\ Fluence\ \left(^{n}/_{cm^2}\right)}{^{32}S(n,p)Cf-eqv}\ x\ 0.563(\pm 2.5\%) \frac{1-MeV(Si)fluence}{Total\ Fluence\ \left(^{n}/_{cm^2}\right)}$$
$$(11)$$

$$\phi_{1-MeV(Si)} = (Nickel\ Activity)\ x\ 3.412\ x\ 10^{10}(\pm 3.1\%) \frac{Total\ Fluence}{\left(^{Bq}/_{g_{Ni}}\right)}\ x\ 0.563(\pm 2.5\%) \frac{1-MeV(Si)fluence}{Total\ Fluence\ \left(^{n}/_{cm^2}\right)}$$
$$(12)$$

VU's pelletron linear accelerator is located in the basement of the Free Electron Laser (FEL) building. It is capable of accelerating light ions to moderate energies with a 1-inch uniform beam diameter. The 4-MeV protons that are used in this work are at the upper bound of its acceleration capabilities. A custom vacuum chamber with an adjustable level stage and various cable feedthroughs enable electronic parts testing at the radiation effects end station. Multiple surface barrier detectors with gold scattering foils are used for dosimetry and observe Rutherford Back Scattering (RBS) with 10% fluence uncertainty [40].

Due to significant scattering of protons by the discrete transistor metal lids, each device must be delidded before irradiation. Three different methods were attempted for delidding devices: acid etch, mechanical erosion, and mechanical separation. Acid etch with nitric acid was ineffective due to the significant lid thickness of each transistor type, even with moderately elevated temperatures. Mechanical erosion with a belt sander and coarse sand paper was the most rapid method with all devices that survived the initial delidding (>95%) remaining functional. Mechanical separation with a can opener-like device custom designed for transistor delidding by Thor was effective and delicate; however, a slower process.

The cobalt-60 arrays in the GIF emit two characteristic gamma rays at 1.17 and 1.33 MeV after beta decay into an excited state nickel-60. Multiple high-activity sources are stored underwater and can be raised into one of several hot cells for irradiation.
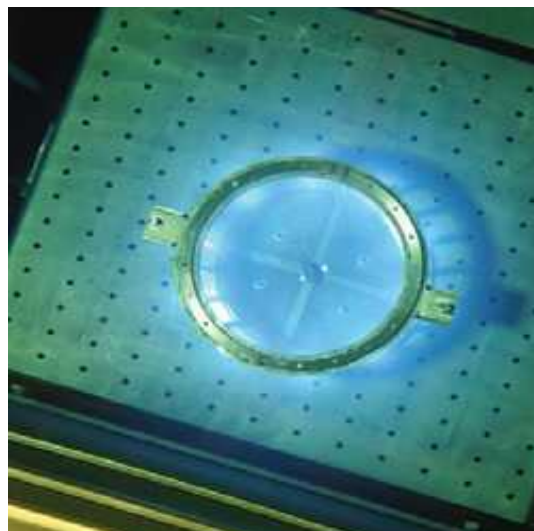
Fig. 19: Gamma irradiation facility high-activity cobalt-60 array. The blue glow is Cherenkov radiation [55].

32

Calibrated ion chamber measurements are made at measured distances from the source for dose and dose rate determination.

The ARACOR x-ray irradiator provides 10 keV x-rays at variable dose rates with an approximate uniform beam diameter of one and a half inches. Dose rate is controlled by a calibration relationship between power source voltage and current. For this experiment series a dose rate of ~30 krad (SiO_2)/min is used with the power source at 35 kV and 30 mA.

Fig. 20 and 21 depict the experimental facilities and experimental setups used at SNL and VU, respectively. In the experiments at SNL, the devices were irradiated passively, mounted in electrostatic foam with dosimetry in close proximity by a spectrum of neutron energies or two cobalt-60 gamma ray energies. In experiments at VU, devices were irradiated while grounded in a DUT board by a single proton or x-ray energy.

In the ACRR experiments for displacement damage sensor evaluation, numerous devices were irradiated at a single time and the ASTM E1855 annealing procedure was performed in its entirety. For irradiations in the pelletron vacuum chamber, the ASTM procedure was performed without stabilization anneals at each fluence level due to the time consuming nature of creating and releasing vacuum conditions in the chamber. This was supplemented with consistent, prompt measurements of I-V characteristics with a standardized readout time between one and two minutes after irradiation. During this time period, rapid annealing of current gain can occur (see Fig. 27), which indicates limited reliability for the displacement damage sensor results obtained. Further investigation is needed of ionizing dose annealing with these parts to determine appropriate stabilization and recovery annealing conditions.

33
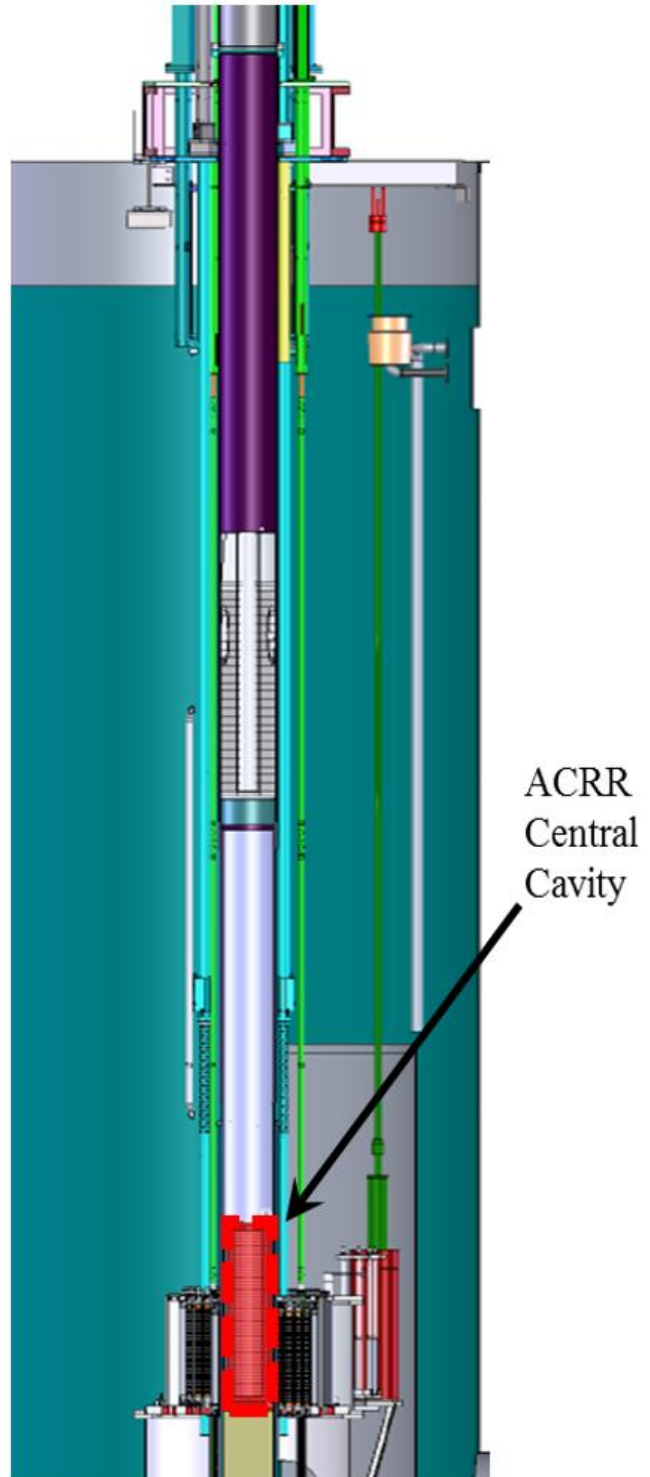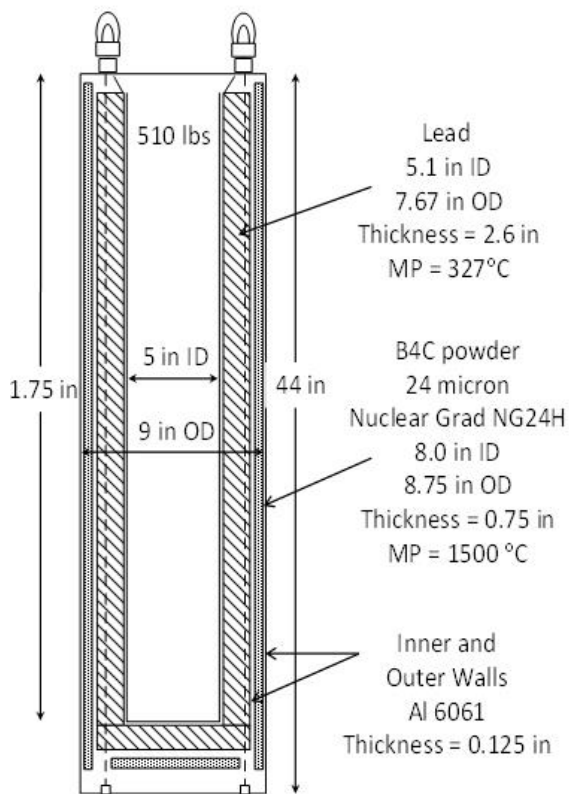
Fig. 20: Two experimenters (Martin and Tonigan) load an experimental package from the top of ACRR central cavity (top left). Schematic of the lead-boron field modifying bucket (bottom left). 3D model of the ACRR with the central experimental cavity highlighted (right). The central cavity is 9 inches in diameter, creating a tight fit for the LB-44 bucket.
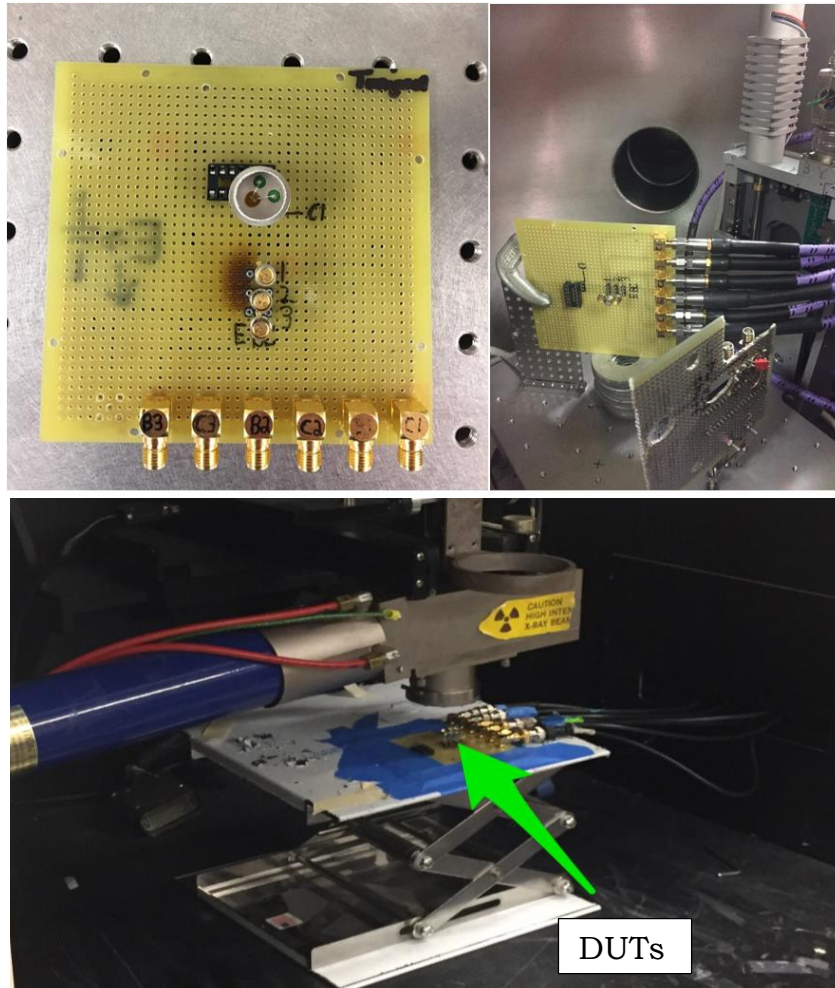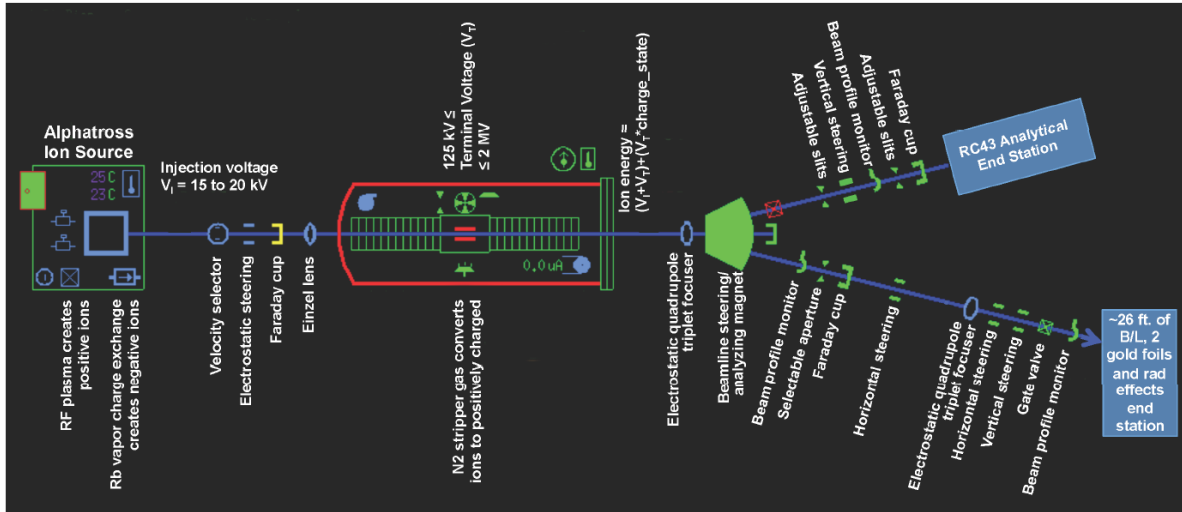
Fig. 21: Schematic of the VU pelletron and beamlines [34]; the radiation effects beamline is used in this work (top). Custom fabricated prototyping board (DUT board) for I-V measurements overhead view (left middle) and board mounted in pelletron beamline (right middle). ARACOR x-ray irradiator with board mounted and DUTs connected.

Chapter IV: Experiment Results

The results obtained in these experiments confirm the opportunity for application of three different types of bipolar transistors as displacement damage sensors for irradiations with two different energetic particles (i.e., proton and neutron). The complete application of the ASTM test method in a neutron environment provides a comparable 1-MeV(Si) equivalent fluence measurement to tradition dosimetry for the 2N2222 and, with increased neutron sensitivity [10], for the 2N1486. An abridged version of the test method with a batch-averaged damage factor was applied to the 2N2484 device. 1-MeV(Si) fluence measurements deduced using this device had greater uncertainty. The general trend of proton degradation to neutron degradation is found to agree with calculated NIEL. The results from an adjusted displacement damage sensor
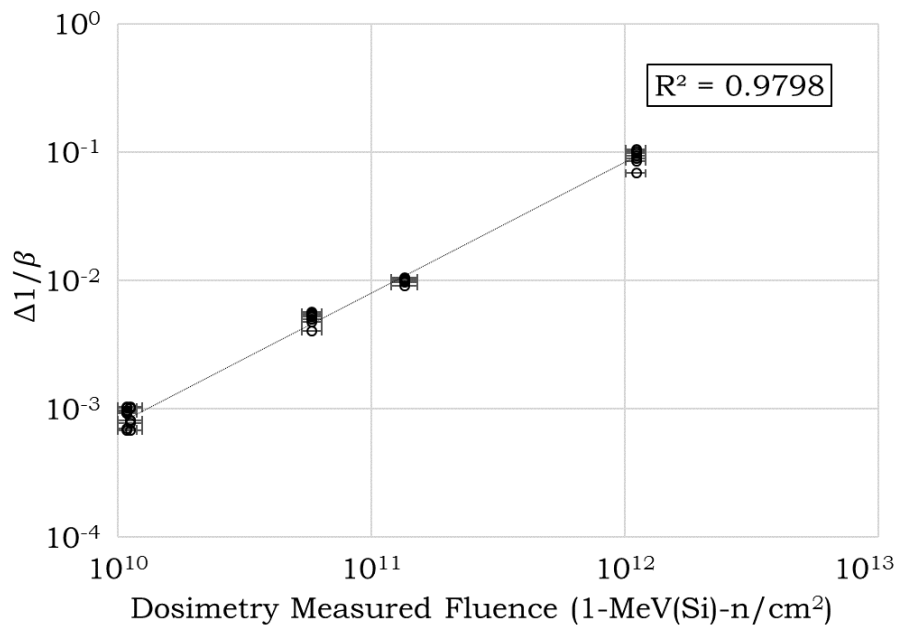
Fig. 22.   Reciprocal current gain degradation vs. neutron fluence for 2N1486 transistors in the ACRR LB-44 environment. The figure contains the response of 51 transistors exposed to five levels of fluence ranging from 1.09×10^{10} to 1.11×10^{12} 1-MeV(Si)-eqv.n/cm^2 as measured by sulfur activation dosimetry. The horizontal error bars represent the uncertainty in each sulfur dosimetry measurement and the individual current gain measurements [10].

procedure provides example 4-MeV proton fluence measurements. The proton fluence measurements only provide order of magnitude accuracy without individual device specific corrections for ionizing dose and with TID annealing readout variability.

The most important relationship to observe for displacement damage sensors is the linearity of reciprocal current gain degradation (or excess base current at a fixed collector current). In Fig. 22, the linearity observed for the 2N1486 transistor is shown at fluences as low as 1×10^{10} 1-MeV(Si) eqv. n/cm^2. Fig. 23 is a log-log plot of reciprocal current gain degradation vs. fluence for 4-MeV proton and neutron irradiations for the three devices (i.e., 2N1486, 2N2484, 2N2222). A linear relationship plotted on a log-log plot will always have a slope of 1 (see bottom left of Fig. 23). Fig. 23 shows the response the three types of transistors is linear in the neutron response range of 1×10^{10} 1-MeV(Si) n/cm^2 to $>1 \times 10^{14}$ 1-MeV(Si) n/cm^2.

A linear response is obtained for the 2N1486, 2N2484, and 2N2222 in a proton response range of 1×10^{10} to $>1 \times 10^{13}$ 4-MeV p/cm^2. For the proton curves, a representative individual device response is plotted over multiple fluence levels, without a stabilization anneal because of the ease of measuring devices frequently during irradiation and the difficulty of irradiating many devices (due to beam size and vacuum pumping). The ratio of proton to neutron degradation for each device is of the same order of magnitude as the corresponding NIEL ratio of 10, with a lower damage factor ratio of 6.1 (2N2484) and an upper damage factor ratio of 15.3 (2N1486). The spread in these ratios is likely due to varying contributions from ionizing dose in the proton irradiations from manufacturing variability (most importantly oxide thickness [21]). The use of device response on a part by part basis in both environments would improve performance predictions and displacement damage sensor accuracy.
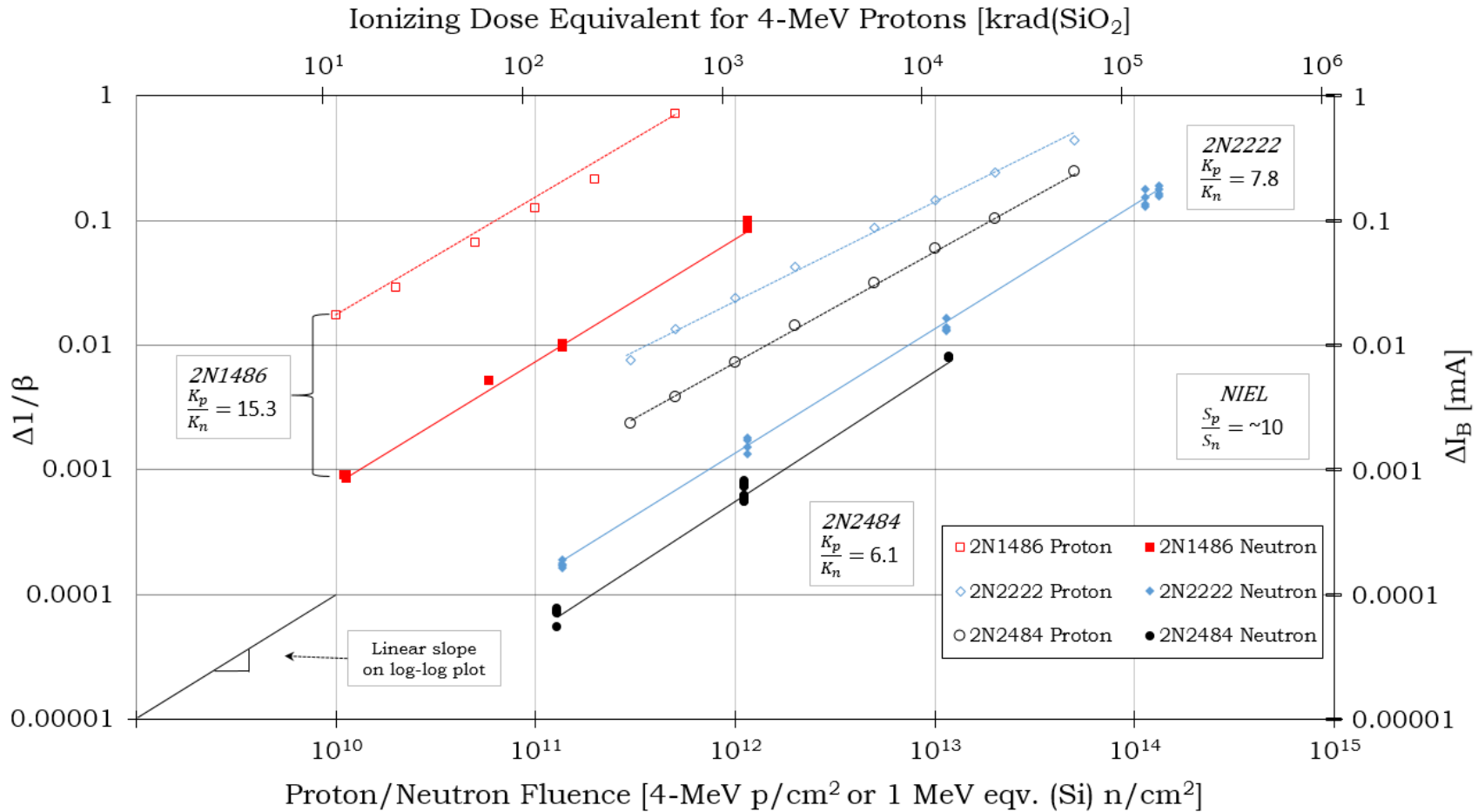
Fig. 23: Reciprocal current gain degradation vs. particle fluence for three types of devices. The secondary y-axis has the excess base current, ΔI_B, and the secondary x-axis has the equivalent ionizing radiation dose for 4-MeV protons. Proton results are corrected for ionizing dose degradation following eq. 16. The ionizing dose equivalence of 4-MeV protons is done following a MRED simulation in [13] with a value of 1.16×10^{-9} krad(SiO$_2$) per proton. A linear relationship plotted on a log-log plot will always have a slope of 1 (i.e. ln(y)= B ln(x) with B=1). B = ~1 for all data sets.

The following section contains details of the device response in each environment and displacement damage sensor measurements. The uncertainty calculation for displacement damage sensor measurements and the adjustment of proton results to account for ionizing radiation is described. The effect of both annealing conditions, stabilization and recovery, is quantified for neutron irradiations.

With a linear response of increasing base current (or reciprocal current gain degradation) with particle fluence confirmed for each device, the standard test method can be used to calculate a damage factor and subsequent displacement damage sensor measured fluence. Table III and IV has measured fluences for the 2N1486 and 2N2222

Table III: 2N1486 1-MeV(Si) eqv. neutron sensor performance

2N1486 DD SENSOR MEASUREMENT COMPARED WITH SULFUR/NICKEL DOSIMETRY	
Sulfur/Nickel Dosimetry	2N1486
$1.13 \times 10^{10} \pm 11\%$	$1.06 \times 10^{10} \pm 11\%$
$1.36 \times 10^{11} \pm 12\%$	$1.10 \times 10^{11} \pm 11\%$
$1.11 \times 10^{12} \pm 9\%$	$1.12 \times 10^{12} \pm 11\%$
Average Damage Factor: $\underline{8.00 \times 10^{-14}}$	

Table IV: 2N2222 1-MeV(Si) eqv. neutron sensor performance

2N2222 DD SENSOR MEASUREMENT COMPARED WITH SULFUR/NICKEL DOSIMETRY	
Sulfur/Nickel Dosimetry	2N2222
$1.16 \times 10^{12} \pm 9\%$	$1.08 \times 10^{12} \pm 9\%$
$1.14 \times 10^{13} \pm 7\%$	$1.08 \times 10^{13} \pm 9\%$
$1.14 \times 10^{14} \pm 4\%$	$1.10 \times 10^{14} \pm 9\%$
*$1.33 \times 10^{14} \pm 6\%$	$1.26 \times 10^{14} \pm 9\%$
$1.24 \times 10^{15} \pm 4\%$	$8.53 \times 10^{14} \pm 9\%$
*$1.07 \times 10^{15} \pm 6\%$	$1.04 \times 10^{15} \pm 9\%$
Average Damage Factor: $\underline{1.11 \times 10^{-15}}$	

*indicates a pulse mode irradiation
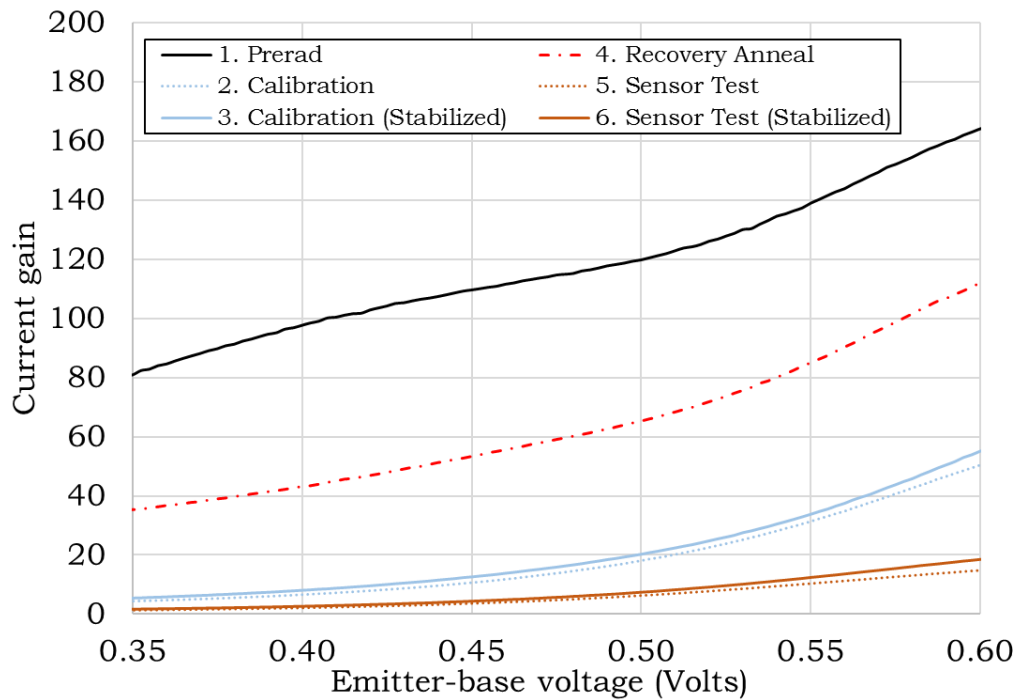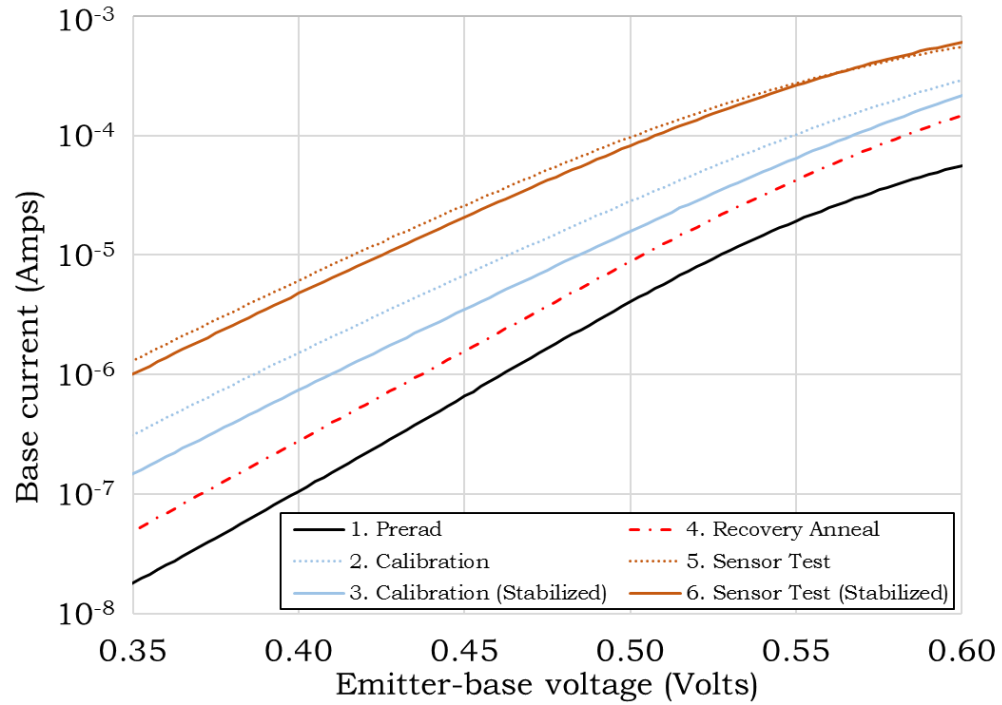
Fig. 24. Base current (upper) and current gain (lower) as a function of emitter-base voltage during each step of the displacement damage sensor procedure. The device response shortly after the calibration and sensor test irradiation is shown as well as after the corresponding stabilization anneals (stabilized). The specific transistor response shown was exposed to a calibration fluence of 3.09×10^{11} 1-MeV(Si)-n/cm^2 and a sensor fluence of 1.08×10^{12} 1-MeV(Si)-n/cm^2 [10].

devices when used as displacement damage sensors compared to the traditional dosimetry fluence measurements (NAA with either sulfur or nickel). The displacement damage sensors provide comparable accuracy to NAA and no significant difference is observable with pulsed irradiations. An example of base current and current gain measurements at each step in the displacement damage sensor procedure can be seen in Fig 24. The irradiation steps (1-2 and 4-5) and recovery anneal step (3-4) displayed the greatest changes in base current and current gain while the stabilization anneal resulted in minor changes. The first stabilization anneal (2-3) recovers more base current than the second stabilization anneal (5-6) for unknown reasons; however, the second stabilization anneal was performed after the device experienced the increased time-temperature recovery anneal.

Assigning an accuracy to a sensor's measured 1-MeV(Si)-equivalent neutron fluence requires knowing the uncertainty of three values:

- Single current gain measurement (σ_{txr})

- Calibration fluence measurement (NAA or other) (σ_D)

- Conversion of calibration dosimetry measurement to 1-MeV(Si) equivalent fluence (spectral adjustment uncertainty) (σ_S)

The spectral adjustment uncertainty from each type of calibration dosimetry (sulfur or nickel) is provided in the LB-44 radiation environment characterization report [49]. The calibration dosimetry uncertainty was provided by facility support staff for each experiment's dosimetry report. To obtain an uncertainty for an individual gain measurement, repeated measurements of transistor gain for both un-irradiated and irradiated devices were performed many times. The combination of nearly 100 repeated measurements on ten 2N1486 transistors (3 pristine transistors and 7 transistors with a range of minor to major gain degradation) demonstrated that the gain measurement

fractional standard deviation was 1.1% or less. The magnitude of the standard deviation decreased with increased current gain degradation. A value of 1.5% is assigned as the relative uncertainty for a representative current gain measurement.

With each contribution to the displacement damage sensor identified in the bullets on the previous page, the total relative uncertainty is found using the following equation based on the component uncertainty contributions being uncorrelated [50].

$$\sigma_{DD\ Sensor,neutron} = \sqrt{\sigma_{txr}^2 + \sigma_D^2 + \sigma_S^2} \tag{13}$$

For proton irradiations, a similar uncertainty can be found using eq. 15, which does not require a spectral adjustment conversion due to the single particle energy.

$$\sigma_{DD\ Sensor,proton} = \sqrt{\sigma_{txr}^2 + \sigma_D^2} \tag{14}$$

The transistor measurement uncertainty is added in quadrature for each current gain measurement performed in the above equations. If desired, a batch-averaged damage factor can be used by including the uncertainty for the device-to-device variation, the standard deviation of the group's measured current gain values is satisfactory if the population is observed to follow a normal distribution (see Fig. 17).

The 2N2484 was irradiated in three different fluence irradiations and provides a good opportunity to observe the efficacy of using a batch-averaged damage factor for a displacement damage sensor measurement. From the first two test level exposures, 1.27 x 10^{11} and 1.11 x 10^{12} 1-MeV(Si) n/cm^2, an average damage factor of 5.80 x 10^{-16} is obtained with an uncertainty of 10% in the calibration dosimetry (sulfur), a batch-fractional standard deviation of 13.2% (number of transistors = 20), and a transistor

current gain measurement uncertainty of 1.5%. The batch-averaged damage factor combined with an average reciprocal current gain degradation of 0.0102 (number of transistors = 5; σ = <1%), produces the sensor measured fluence in the third irradiation of $1.75 \times 10^{13} \pm 16.6\%$ 1-MeV(Si) n/cm^2 compared to the dosimetry measured fluence $1.18 \times 10^{13} \pm 6\%$. The relatively high uncertainty is due to the use of a batch-averaged damage factor with a small batch size (15 transistors); however, the measurement provides a reasonable 1-MeV(Si) equivalent neutron fluence measurement.

Table V-VII contains sample results for the use of each transistor type as a displacement damage sensor in 4-MeV proton irradiations at the VU pelletron. For these measurements, a damage factor is calculated after the first irradiation and then applied (eq. 10 and 11) to each subsequent irradiation and compared with the RBS detector measured fluence. The most accurate example device predictions are presented. Select other devices performed poorly as sensors with results differing from RBS dosimetry as much as an order of magnitude. Rapid room temperature annealing could account for results obtained from devices that deviated from RBS, despite a controlled readout time.

It is desirable to relate the proton and neutron irradiations based upon their calculated NIEL values. A calculated NIEL value for neutrons in silicon is 2.04×10^{-3} MeV-cm^2/g [14] and for 4-MeV protons in silicon is 1.42×10^{-2} MeV-cm^2/g [17], making the corresponding NIEL ratio approximately ~7 or on the order of magnitude of 10^1. NIEL captures the relative sensitivity to particle radiation of the devices used in this work, with each being significantly more sensitive to 4-MeV protons. Corresponding damage factor ratios for each device are seen in Fig. 23 and demonstrate that NIEL provides accurate order of magnitude estimation.

Table V: 2N1486 4-MeV proton sensor performance

2N1486 DD Sensor measurement compared with RBS Measurement

RBS Fluence	2N1486
$2.47 \times 10^{10} \pm 10\%$	$2.56 \times 10^{10} \pm 10.5\%$
$5.54 \times 10^{10} \pm 10\%$	$5.38 \times 10^{10} \pm 10.5\%$
$1.06 \times 10^{11} \pm 10\%$	$8.04 \times 10^{10} \pm 10.5\%$
$2.07 \times 10^{11} \pm 10\%$	$1.33 \times 10^{11} \pm 10.5\%$
$5.09 \times 10^{11} \pm 10\%$	$6.05 \times 10^{11} \pm 10.5\%$
Adj. Device Damage Factor: $\underline{1.22 \times 10^{-12}}$	

Table VI: 2N2222 4-MeV proton sensor performance

2N2222 DD Sensor measurement compared with RBS Measurement

RBS Fluence	2N2222
$2.91 \times 10^{11} \pm 10\%$	$2.45 \times 10^{11} \pm 10.5\%$
$5.06 \times 10^{11} \pm 10\%$	$4.55 \times 10^{11} \pm 10.5\%$
$1.02 \times 10^{12} \pm 10\%$	$8.44 \times 10^{11} \pm 10.5\%$
$2.07 \times 10^{12} \pm 10\%$	$2.07 \times 10^{12} \pm 10.5\%$
$5.05 \times 10^{12} \pm 10\%$	$4.93 \times 10^{12} \pm 10.5\%$
$1.01 \times 10^{13} \pm 10\%$	$1.18 \times 10^{13} \pm 10.5\%$
Adj. Device Damage Factor: $\underline{2.73 \times 10^{-14}}$	

Table VII: 2N2484 4-MeV proton sensor performance

2N2484 DD Sensor measurement compared with RBS Measurement

RBS Fluence	2N2484
$1.02 \times 10^{12} \pm 10\%$	$1.20 \times 10^{12} \pm 10.5\%$
$2.02 \times 10^{12} \pm 10\%$	$2.59 \times 10^{12} \pm 10.5\%$
$5.05 \times 10^{12} \pm 10\%$	$5.91 \times 10^{12} \pm 10.5\%$
$1.01 \times 10^{13} \pm 10\%$	$1.12 \times 10^{13} \pm 10.5\%$
$2.01 \times 10^{13} \pm 10\%$	$1.90 \times 10^{13} \pm 10.5\%$
$5.01 \times 10^{13} \pm 10\%$	$5.17 \times 10^{13} \pm 10.5\%$
Adj. Device Damage Factor: $\underline{1.36 \times 10^{-15}}$	

The 4-MeV proton results are corrected for ionizing dose degradation according to eq. 16 [17]. Proton irradiation creates significant ionizing dose which must be accounted for to isolate the non-ionizing displacement damage.

$$\Delta I_{B(DD,protons)} = \Delta I_{B(total,protons)} - (\Delta I_{B(TID,X-rays)} \text{ x CYR}) \tag{15}$$

where $\Delta I_{B(DD,protons)}$ is the excess base current introduced by proton displacement damage, $\Delta I_{B(total,protons)}$ is the excess base current introduced by ionizing and non-ionizing processes due to protons, $\Delta I_{B(TID,X-rays)}$ is the excess base current introduced in an x-ray irradiation at an equivalent ionizing dose, and CYR is the charge yield ratio between 4-MeV protons and 10 keV X-rays.

As discussed in Section II.C, charge yield can vary between ionizing radiation sources. Due to similarity is stopping power, 20-MeV protons and 10-keV x-rays are typically estimated to have the same charge yield [17] [34] [51] [52]. Based on Fig. 9 in Section II.C., the CYR between 20-MeV protons/10 keV x-rays and 4-MeV protons is approximately 0.54, confirmed in [17]. The charge yield ratio between 10-keV x-rays and cobalt-60 gamma rays was 0.48 (σ = 10%, see Fig. 25) if averaged over the linear range (0.4-0.6 V); however, this ratio varied part to part and its reliability is suspect due to inadequate control of measurement readout time/conditions during the cobalt-60 and 10 keV x-ray irradiations. However, this charge yield is comparable to what has been obtained in other experiments for an unbiased bipolar transistor [33] [38]. In all un-biased charge yield studies, cobalt-60 irradiations produced more excess base current than 10 keV x-rays when compared at the same ionizing dose [32] [33] [51].

The following equation for CYR can be used in eq. 16 if using the ionizing radiation response in the cobalt irradiations. The single value of 0.54 CYR is used with

the Aracor ionizing radiation response. Both methods yield comparable results with only order of magnitude accuracy and significant variability. An especially hard 2N1486 transistor outlier experienced no significant gain degradation by 100 krad(SiO$_2$) in x-ray irradiations, an order of magnitude higher than any other. Base current measurements of pristine devices were more sensitive to ionizing radiation dose than devices previously irradiated in the ACRR (Fig. 26).

$$CYR = \frac{\Delta I_{B,4-\text{MeV protons}}}{\Delta I_{B,Cobalt-60}} = \frac{\Delta I_{B,4-\text{MeV protons}}}{\Delta I_{B,10-keV\ X-ray\backslash 20-MeV\ Protons}}\ x\ \frac{\Delta I_{B,10-keV\ X-rays}}{\Delta I_{B,Cobalt-60}} \quad (16)$$

The similarity of excess base current introduced by 4-MeV protons and approximately an order of magnitude more 1-MeV(Si) equivalent neutrons in a characteristic 2N1486 BJT is shown in Fig. 27, supporting this conclusion and the calculated NIEL ratio of ~10^1.
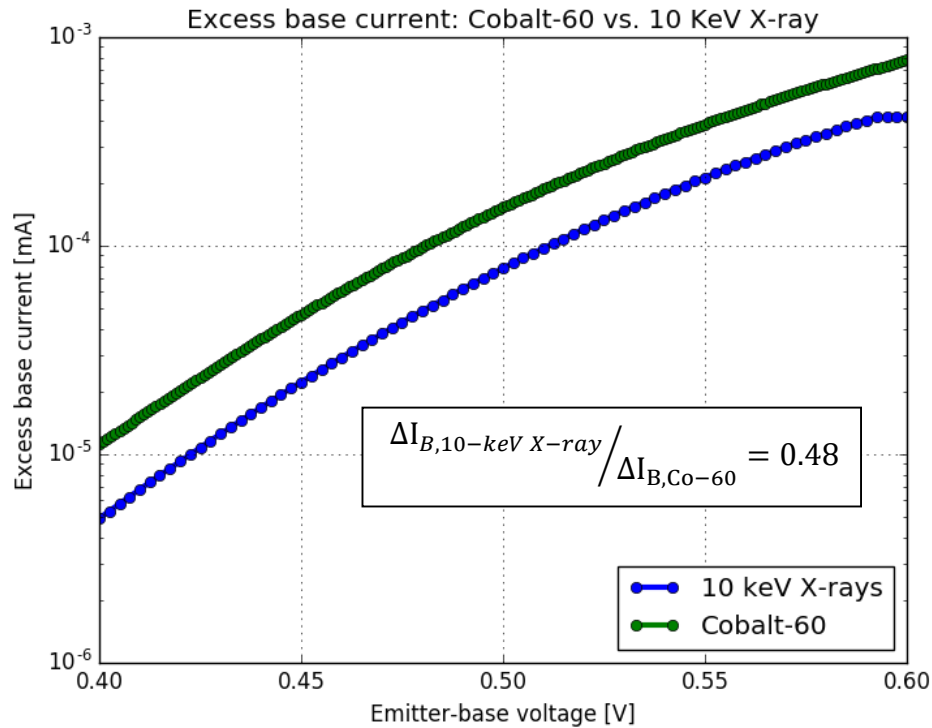
Fig. 25: Excess base current from an equivalent ionizing radiation dose of cobalt-60 and 10-keV x-ray irradiations of 500 krad(SiO$_2$) in a sample 2N1486 transistor. Results varied significantly from part-to-part.
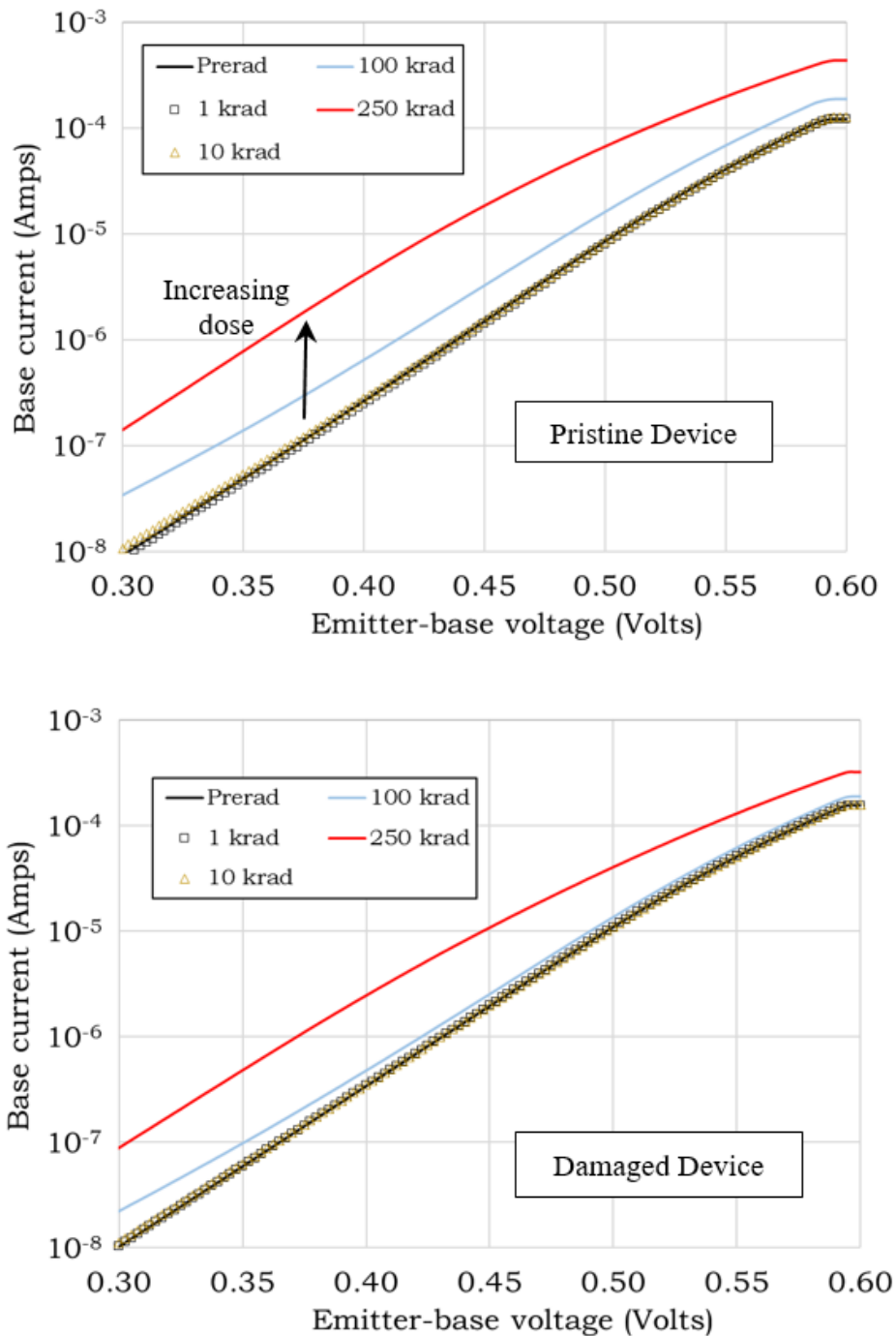
Fig. 26. Base current in a previously (upper) un-irradiated and irradiated (lower) 2N1486 transistor as a function of emitter-base voltage with each curve representing a different gamma radiation dose. The irradiated device was exposed to 1.16×10^{10} 1-MeV(Si)-n/cm^2. The prerad, 1 krad(Si) and 10 krad(Si) data curves overlap in both figures. While the worst case bias (reverse bias on emitter) [33] was not placed on the device for the GIF experiment, the onset of ionizing dose effects occur at greater than an order of magnitude higher dose than was experienced in the ACRR-neutron experiments.
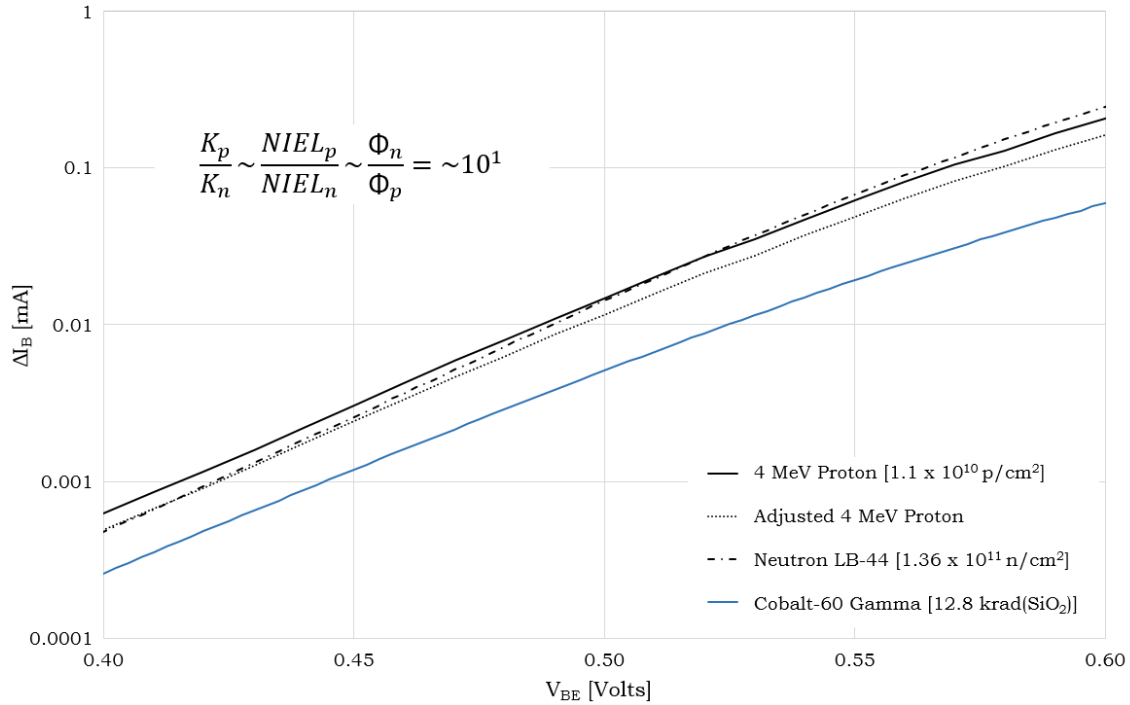
Fig. 27: Excess base current vs. base-emitter applied voltage for two representative 2N1486 transistors irradiated by an order of magnitude more neutrons in the ACRR (LB-44) than 4-MeV protons. The excess base current from a cobalt-60 irradiation is displayed at an equivalent dose level corresponding to the 4-MeV protons. The ideality factor of the proton-irradiated device is greater than that of the neutron-irradiated device (reduced slope). This effect is most likely due to an increased contribution of recombination in the emitter-base depletion region (n=2), an area that spreads with increased oxide trapped charge associated with proton ionization [19] [33] [35].

Two annealing conditions are called for in the ASTM E1855 procedure, a stabilization anneal (2 hours/350 K) and a recovery anneal (24 hours/450 K). The stabilization anneal is intended to provide a stable current gain measurement regardless of measurement time and that is equivalent to the current gain if measured an infinite time after irradiation. Fig. 28 contains the room temperature annealing of current gain for all three devices compared to the average stabilization current gain recovery. The annealing at room temperature is rapid for the first ~30 minutes regardless of the amount of degradation; however, the most degraded devices experienced the largest
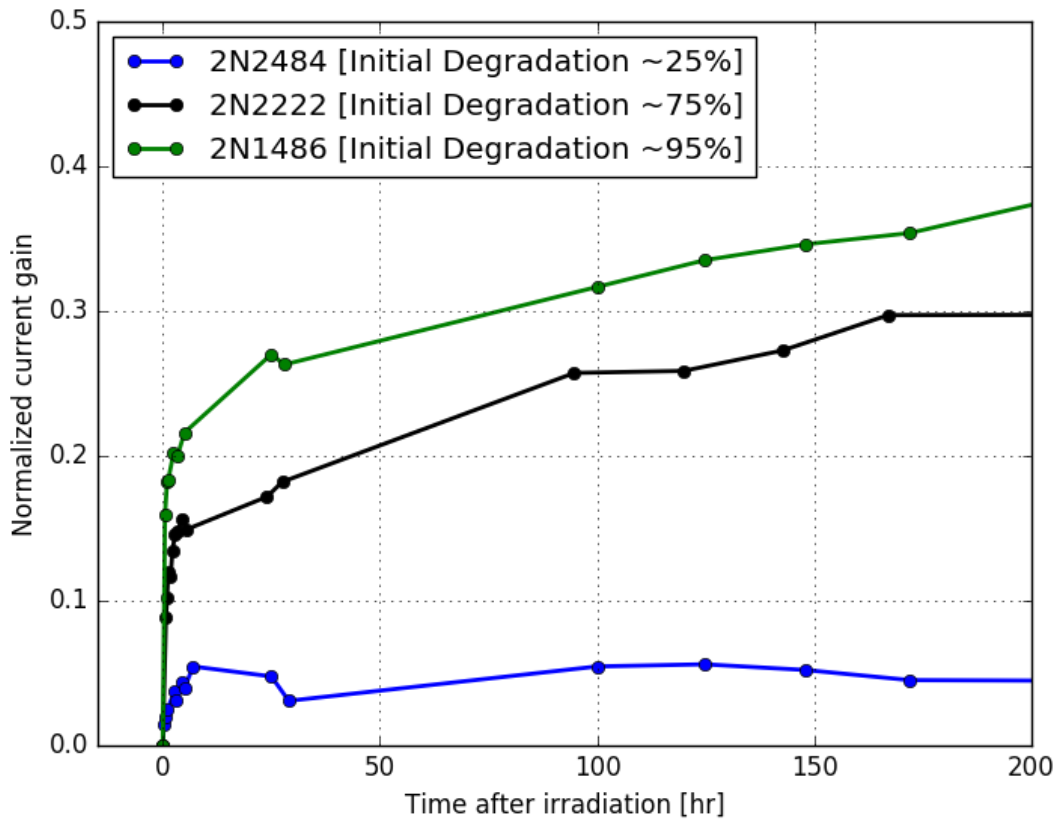
Fig. 28: Current gain measurement displaying room temperature annealing of degradation. The stabilization anneal usually restores ~10% of the degraded current gain, which is the approximate long time current gain room temperature annealing recovery for the two less damaged devices when taking the initial measurement at ~30 minutes.

percent current gain recovery. Measurements taken 70 days after irradiation (~1700 hours) recovered approximately 10% current gain from the first post-irradiation measurement without stabilization annealing.

The recovery anneal in ASTM E1855 calls for 24 hours at 450 K. If the temperature increases 30 K, no appreciable increase in annealing occurs. However, if the temperature decreases 30 K, significantly less annealing occurs. The majority of current gain recovery occurs within the first six hours (Fig. 29).
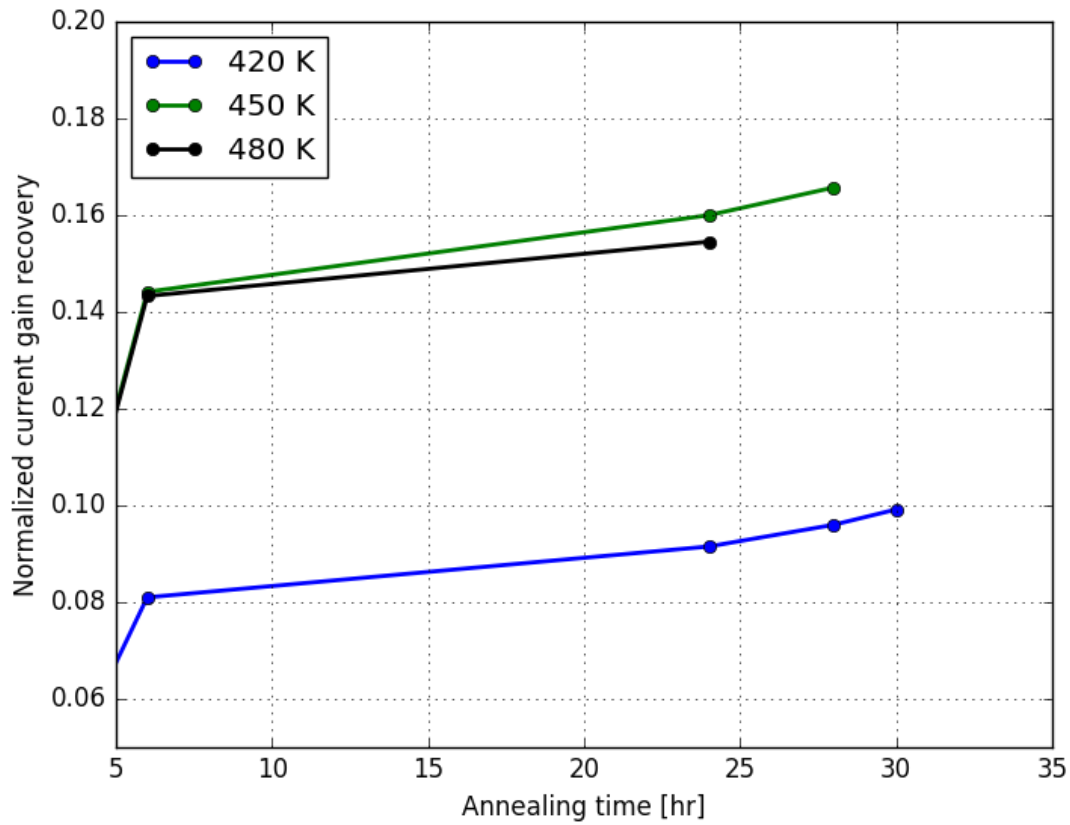
Fig. 29: Elevated temperature annealing performed on lightly damaged 2N2484 devices, more significant annealing has been observed in more heavily degraded devices. Increasing the temperature above 450 K doesn't result in more annealing however decreasing the temperature below 450 K results in significantly less. This indicates the 420 K annealing temperature of VP [22] must be surpassed. The annealing is most significant in the first 6 hours and marginal annealing occurs after 24 hours.

Chapter V: Discussion

The Messenger-Spratt equation has been used to describe the gain degradation of BJTs for over 50 years. It is applied in this work to describe the behavior of BJTs used as displacement damage sensors for multiple device types. The majority of devices yield comparable accuracy to traditional dosimetry in proton and neutron environments. Part-to-part response and annealing rate variability are complicated by the following considerations.

Protons lose energy from linear energy transfer (LET) continuously while passing through a material. Protons have a sharply peaked Bragg curve, with the majority of energy deposition happening at the end of range. Messenger et. al [53] pointed out that if the thickness of a target region is large compared to the incident particle range,
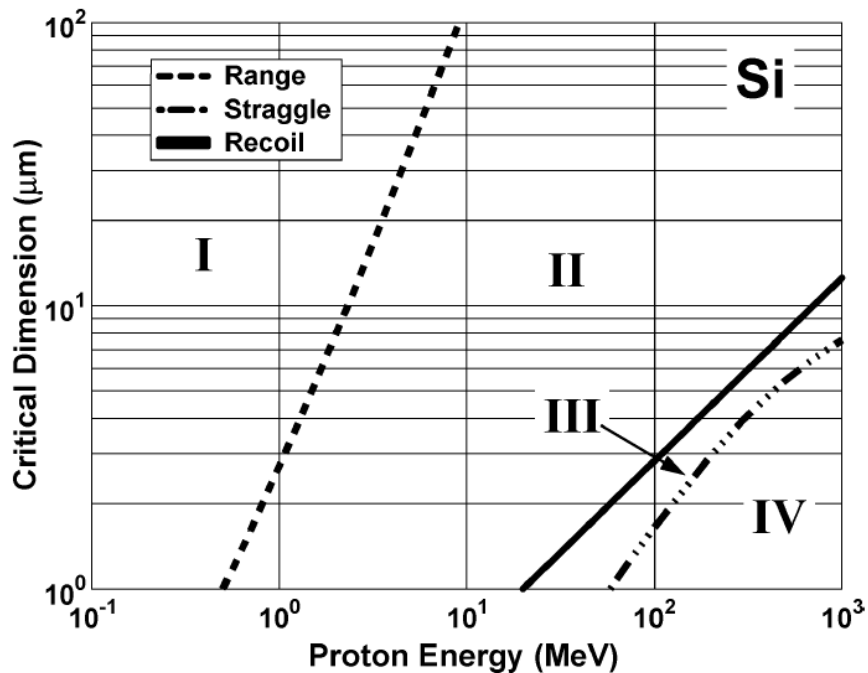
Fig. 30: Regions where NIEL does (II) and does not (I,III,IV) provide an accurate estimate of the energy deposition and defect generation in silicon due to different particle/crystal interactions [53].

51

substantial changes in the NIEL result in non-uniform damage. The proton energy and device dimensions they recommend to avoid this complication lie in region II of Fig. 30. The large base width device, the 2N1486, is right at the border of this region for 4-MeV protons, suggesting NIEL may be in a variable regime of where finite particle range and non-uniform damage is a concern. The 2N2222 and 2N2484 have critical dimensions less than 10^1 μm, placing them safely in region II for a 4-MeV proton irradiation.

In studies by Fleming et al, silicon defect type variety and clustering that occur with energetic particle bombardment are investigated with deep-level transient spectroscopy (DLTS). Clustered defects created by PKAs (see Fig. 31) enable the formation of significantly more complex defect types with chains of vacancies, interstitials, and impurities combining to create unique electronic states within the forbidden bandgap. The complex transport of charge carriers through
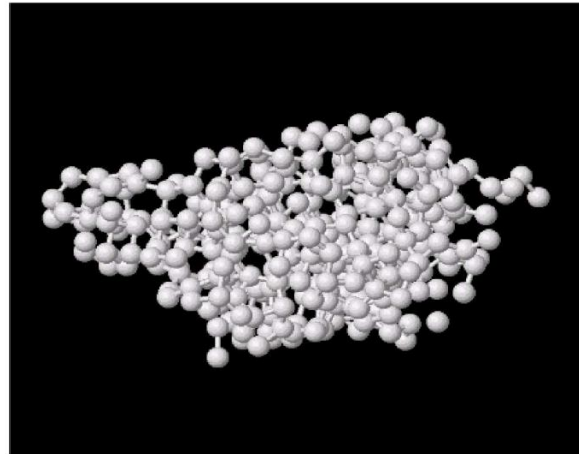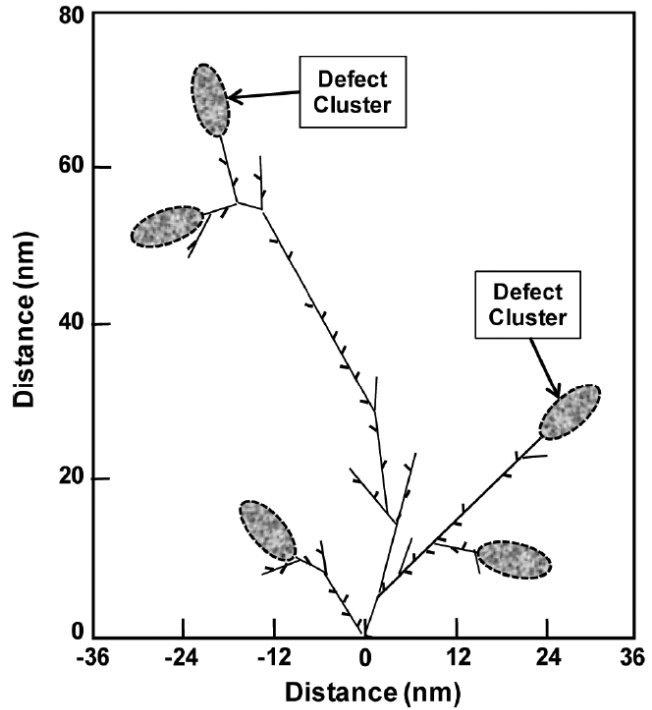
Fig. 31: Formation of defect clusters from an incident particle at (0,0) (upper) Each clustered region stems from a single PKA collision and the line stemming to clusters contain individual frenkel pairs. MD simulation of a defect cluster behaving as an amorphous grain (lower) [27].

large disordered regions, which can be seen as amorphous grains (Fig. 31, bottom), encouraged early researchers to treat them as space-charge regions in modeling. The Gossick cluster model [54] was an early attempt at modeling this; however, the extent of cluster size was assumed to be far larger than found in later silicon cluster studies [22]. The Gossick cluster model assumed disordered regions to be greater than or equal to 100 nm in width, whereas actual cluster diameters are found to be ≤ 5 nm [22].

Defects can act as more than recombination traps. Fig. 32 shows multiple ways that defects can affect charge carrier transport, including thermal generation, temporary trapping, and majority carrier trapping. In addition to the Fig. 32 examples impurity type conversion can occur, switching donor-like behavior to acceptor-like and vice versa. The same defects types can be present in different charge states. Fleming highlights
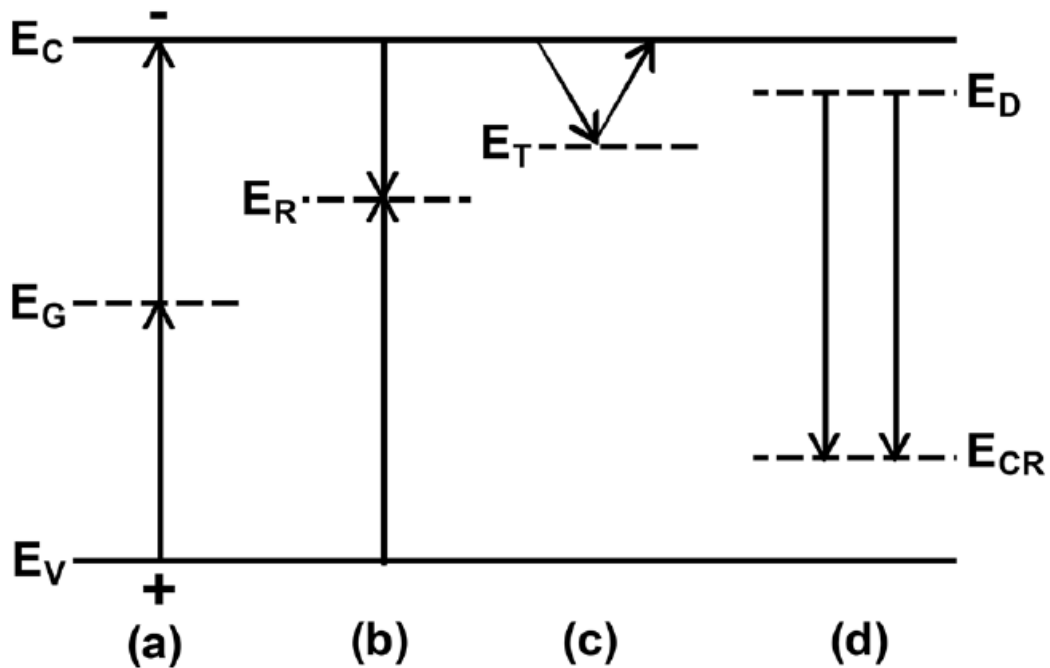
Fig. 32: Defect states created within the silicon forbidden band gap and their effect on charge carriers. (a) represents the thermal generation of carriers, (b) carrier recombination, (c) temporary trapping, and (d) reduction of majority carrier [27].

that, although the damage factor metric remains valid, it is important to recognize the assumption that recombination traps are assumed to be uniformly distributed and dominantly act like recombination centers [29]. This assumption enables eq. 18 –the backbone assumption of this work- that the increased concentration of all trap types is directly proportional to the minority carrier degradation [26]:

$$\frac{1}{\Delta\tau} = \frac{1}{\tau_\Phi} - \frac{1}{\tau_0} = \sigma v_{th} \Delta N_T \qquad (17)$$

where τ_0 is the pristine device minority carrier lifetime, τ_Φ is the minority carrier lifetime after irradiation, σ is the carrier capture cross-section, v_{th} is the carrier thermal velocity, and ΔN_T is the increase in recombination traps.

In addition to the stochastic variability in NIEL by protons and neutrons and the assumptions regarding defect types, significant ionizing radiation dose can result in non-linear combined ionizing and displacement damage degradation. This effect is described by Barnaby, et al. and leads to enhanced gain degradation in NPN transistors in proton irradiations [20]. Non-linear degradation occurs with proton irradiation because ionization-induced defects (in the oxide and at the interface) affect the recombination rate in the bulk silicon. Surface recombination velocity, from the addition of ionization-induced defects, and sub-surface bulk recombination, from displacement damage defects, have been shown to be non-linearly correlated [20]. Although confirming this enhancement is beyond the scope of this thesis and requires device modeling to analyze, combined effects could have contributed to the variability of proton displacement damage sensor measurements.

Recently, an improved Messenger-Spratt equation was presented by Barnaby, et al. [26]. This modification addresses a simplification in the original equation where only

the excess base current from bulk recombination (ΔI_{B2} in Fig. 2) is appropriately considered. ΔI_{B3} and minority carrier degradation due to recombination in the emitter-base depletion region are related with different factors than bulk recombination (eq. 7 vs. eq. 8). This effect is dominant at low biases where emitter-base recombination plays a more significant role. The reference collector current of 1 mA used in this work, which occurs above low applied bias, sufficiently mitigates the effect of this correction on damage factor calculations.

The preceding complications and complexities are reduced by the use of individual device's responses (or well defined batch parameters), thoroughly characterized environments, and the elevated temperature anneals that place readout in stable temporal regimes. The use of an individual device for quantifying damage factors and a CYR removes the process variation variables from device-to-device. Measurements in unknown environments can be conducted with calibrated devices; however, results should be taken with a degree of skepticism if substantial ionizing radiation dose is anticipated. Further investigation in the device specific time-temperature dependent annealing of ionizing radiation effects could remedy the variability with proton irradiations.

In addition to the complications discussed in this section, the measurement accuracy can be affected by mechanical or chemical damage, which must be avoided by careful handling of the devices. If devices are properly secured during irradiation and stored in a sealed container with anti-static foam these types of damage are avoidable.

Chapter VI: Conclusion

This thesis presents the 2N1486 transistor as a high sensitivity displacement damage sensor and demonstrates that the correlation of proton and neutron displacement damage is described adequately by NIEL for three different bipolar device types. The 2N1486, 2N2484, and 2N2222 displacement damage sensors are further applied with a modified procedure to approximate 4-MeV proton fluence. A batch-averaged displacement damage sensor approach is examined with the 2N2484 transistor and provides 1-MeV(Si) eqv. neutron fluence measurements with higher uncertainty. The batch-average approach is useful because it allows pristine transistors to be used in test-level measurements without prior calibration.

The complicated nature of displacement damage is discussed and the validity of the damage factor metric is verified. The annealing conditions in ASTM E1855 are investigated, confirming that 24 hours at 450 K is an appropriate recovery anneal condition. The stabilization anneal condition is confirmed to replicate the long term room temperature annealing behavior of the three transistors.

Further investigation of the annealing of ionizing radiation degradation is needed to improve the quality of the displacement damage sensor approach for proton irradiations. Device-to-device variability can be an issue, but the use of averaged responses over multiple devices helps deal with this. The displacement damage sensor methodology successfully estimates particle fluence based on degradation but does not reveal the fundamental material changes that occur; computational modeling and improved defect-specific diagnostics are needed to fully capture device response behaviors.

The application of the 2N1486 as a displacement damage sensor has been successfully applied at HEDP facilities such as the National Ignition Facility, University of Rochester Omega facility, and SNL's Z-Machine. The drafting of a new standard test method with the higher sensitivity 2N1486 has been initiated with the ASTM E10: *Nuclear Technology and Applications* Committee.

REFERENCES

[1]   S. Glasstone and P. Dolan, "The effects of nuclear weapons," United States Department of Defense, Washington, D.C., 1977.

[2]   J. L. Barth, C. S. Dyer, and S. G. Stassinopoulos, "Space, atmospheric, and terrestrial radiation environments," *IEEE Trans. Nucl. Sci.,* vol. 50, no. 3, pp. 466-482, June 2003.

[3]   J. G. Kelly, P. J. Griffin, and T. F. Luera, "Use of silicon bipolar transistors as sensors for neutron energy spectra determinations," *IEEE Trans. Nucl. Sci.,* vol. 38, no. 6, pp. 1180-1186, December 1991.

[4]   "E722-14: Standard practice for characterizing neutron fluence spectra in terms of an equivalent monoenergetic neutron fluence for radiation-hardness testing of electronics," *ASTM Interational,* 2014.

[5]   "E1855-15: Standard test method for use of 2N2222A silicon bipolar transistors as neutron spectrum sensors and displacement damage monitors," *ASTM International,* 2015.

[6]   "E261-15: Standard practice for determining neutron fluence, fluence Rate, and spectra by radioactivation techniques," *ASTM International,* 2015.

[7]   C. A. Coverdale, C. Deeney, A. L. Velikovich, R. W. Clark, Y. K. Chong, J. Davis, J. Hittenden, C. L. Ruiz, G. W. Cooper, A. J. Nelson, J. Franklin, P. D. LePell, J. P. Apruzese, J. Levine, J. Banister, and N. Qi, "Neutron production and implosion characteristics of a deuterium gas-puff Z pinch," *Phys. Plasmas,* 2007.

[8]   H. -S. Park, O. A. Hurricane, D. A. Callahan, D. T. Casey, E. L. Dewald, T. R. Dittrich, T. Döppner, D. E. Hinkel, L. F. Berzak Hopkins, S. Le Pape, T. Ma, P. K. Patel, B. A. Remington, H. F. Robey, and J. D. Salmonson, "High-Adiabat High-Foot Inertial Confinement Fusion Implosion Experiments on the National Ignition Facility," *Phys. Rev. Letters,* 2014.

[9]   G. L. Messenger and J. P. Spratt, "The effects of neutron irradiation on germanium and silicon," *Proceedings of the IRE,* vol. 46, pp. 1038-1044, June 1958.

[10]   A. M. Tonigan, E. J. Parma, and W. J. Martin, "The Development of High Sensitivity Neutron Displacement Damage Sensor," *IEEE Trans. Nucl. Sci.,* p. (in press), Jan. 2017.

[11]   P. J. Griffin, D. B. King, and N. R. Kolb, "Application of spallation neutron sources in support of radiation hardness studies," *Nucl. Inst. & Meth. Phys.,* pp. 684-687, 2006.

[12] B. Mukherjee, "Development of a single neutron irradiation facility with variable average energy using a light water moderated AmBe source," *Nucl. Inst. & Meth. in Phys.,* vol. 363, pp. 616-618, 1995.

[13] J. De La Cova, W. Gilbert, M. Graham, J. Kilgore, I. Krokvist, R. Rusack, R. Schwienhorst, J. Sielaff, D. Sievers, and T. Vidnovic III, "A Ca-252 neutron irradiator for testing electronic components for the large hadron collider," *IEEE Nucl. Sci. Symp.* , November 2001.

[14] G. P. Summers, E. A. Burke, C. J. Dale, E. A. Wolicki, P. W. Marshall, and M. A. Gehlhausen, "Correlation of particle-induced displacement damage in silicon," *IEEE Trans. Nucl. Sci.,* vol. 34, no. 6, pp. 1134-1139, December 1987.

[15] International Atomic Energy Agency, "Decommissioning techniques for research reactors," IAEA-TECDOC-1273, Vienna, Austria, 2002.

[16] E. Bielejec, G. Vizkelethy, N. R. Kolb, D. B. King, and B. L. Doyle, "Metrics for comparison between displacement damage due ion beam and neutron irradiation in silicon bjts," *IEEE Trans. Nucl. Sci.,* vol. 54, no. 6, pp. 2282-2287, Dec. 2007.

[17] C. N. Arutt, K. M. Warren, R. D. Schrimpf, R. A. Weller, J. S. Kaupplila, J. D. Rowe, A. L. Sternberg, R. A. Reed, D. R. Ball, and D. M. Fleetwood, "Proton irradiation as a screen for displacement damage sensitivity in bipolar junction transistors," *IEEE Trans. Nucl. Sci.,* vol. 62, no. 6, pp. 2498-2504, December 2015.

[18] R. S. Muller and T. I. Kamins, *Device Electronics for Integrated Circuits*, New York: Wiley & Sons, 2003.

[19] R. D. Schrimpf, "Gain degradation and enhanced low-dose-rate sensitivity in bipolar junction transistors," *International Journal of High Speed Electronics and Systems,* vol. 14, no. 2, 2004.

[20] H. J. Barnaby, R. D. Schrimpf, A. L. Sternberg, V. Berthe, C. R. Cirba, and R. L. Pease, "Proton radiation response mechanisms in bipolar analog circuits," *IEEE Trans. Nucl. Sci.,* vol. 48, no. 6, pp. 2074-2080, Dec. 2001.

[21] D. M. Fleetwood, "Total ionizing dose effects in MOS and low-dose-rate-sensitive linear-bipolar devices," *IEEE Trans. Nucl. Sci.,* vol. 60, no. 3, pp. 1706-1730, June 2013.

[22] J. Srour, C. J. Marshall, and P. W. Marshall, "Review of displacement damage effects in silicon devices," *IEEE Trans. Nucl. Sci.,* vol. 50, no. 3, pp. 653-670, June 2003.

[23] E. P. Wigner, "Theoretical physics in the metallurgical laboratory of chicago," *Jour. Appl. Phys.,* vol. 17, no. 11, November 1946.

[24] G. H. Kinchin and R. S. Pease, *The displacement of atoms in solids by radiation*, Harwell, Didcot, Berks, 1955.

[25] R. E. Davis, W. E. Johnson, K. Lark-Horovitz, and S. Siegel, "Nucleon bombarded germanium semiconductors," Atomic Energy Commission, Oak Ridge, TN, USA., 1948.

[26] H. J. Barnaby, R. D. Schrimpf, K. F. Galloway, X. Li, J. Yang, and C. Liu, "Displacement damage in bipolar junction transistors: beyond messenger-spratt," *IEEE Trans. Nucl. Sci.,* vol. 64, no. 1, pp. 149-155, September 2016.

[27] J. R. Srour and J. W. Palko, "Displacement damage effects in irradiated semiconductor devices," *IEEE Trans. Nucl. Sci.,* vol. 60, no. 3, pp. 1740-1766, June 2013.

[28] C. J. Dale, P. W. Marshall, E. A. Burke, G. P. Summers, and E. A. Wolicki, "High energy electron induced displacement damage in silicon," *IEEE Trans. Nucl. Sci.,* vol. 35, no. 6, pp. 1208-1214, December 1988.

[29] R. M. Fleming, C. H. Seager, D. V. Lang, and J. M. Campbell, "Defect annealing in neutron and ion damaged silicon: influence of defect clusters and doping," *Jour. Appl. Phys.,* vol. 107, 2010.

[30] R. M. Fleming, C. H. Seager, D. V. Lang, P. J. Cooper, E. Bielejec, and J. M. Campbell, "Effects of clustering on the properties of defects in neutron irradiated silicon," *Journal of Applied Physics,* vol. 102, 2007.

[31] E. Bielejec, G. Vizkelethy, N. R. Kolb, D. B. King, and B. L. Doyle, "Damage equivalence of heavy ions in silicon bipolar junction transistors," *IEEE Trans. Nucl. Sci.,* vol. 53, no. 6, pp. 3681-3686, December 2006.

[32] R. L. Pease, "Total ionizing dose effects in bipolar devices and circuits," *IEEE Trans. Nucl. Sci.,* vol. 50, no. 3, pp. 539-551, June 2003.

[33] R. N. Nowlin, E. W. Enlow, R. D. Schrimpf, and W. E. Combs, "Trends in the total-dose response of modern bipolar transistors," *IEEE Trans. Nucl. Sci.,* vol. 39, no. 6, pp. 2026-2035, December 1992.

[34] J. R. Schwank, M. R. Shaneyfelt, D. M. Fleetwood, J. A. Felix, P. E. Dodd, P. Paillet, V. Ferlet-Cavrois, "Radiation effects in MOS oxides," *IEEE Trans. Nucl. Sci.,* vol. 55, no. 4, pp. 1833-1853, August 2008.

[35] H. J. Barnaby, S. K. Smith, R. D. Schrimpf, D. M. Fleetwood, and R. L. Pease, "Analytical model for proton radiation effects in bipolar devices," *IEEE Trans. Nucl. Sci.,* vol. 49, no. 6, pp. 2643-2649, December 2002.

[36] T. R. Oldham, "Analysis of damage in MOS devices for several radiation environments," *IEEE Trans. Nucl. Sci.,* vol. 31, no. 6, pp. 1236-1241, December 1984.

[37] E. W. Enlow, R. L. Pease, W. E. Combs, R. D. Schrimpf, and R. N. Nowlin, "Response of advanced bipolar processes to ionizing radiation," *IEEE Trans. Nucl. Sci.,* vol. 38, no. 6, pp. 1342-1351, December 1991.

[38] M. R. Shaneyfelt, D. M. Fleetwood, J. R. Schwank, and K. L. Hughes, "Charge yield for cobalt-60 and 10-keV x-ray irradiations of MOS devices," *IEEE Trans. Nucl. Sci.,* vol. 38, no. 6, pp. 1187-1194, December 1991.

[39] Sandia National Laboratories Radiation Facilities. [Online]. Available: http://www.sandia.gov/research/research_foundations/radiation_effects_high_ene rgy_density_science.html

[40] M. W. McCurdy, M. H. Mendenhall, R. A. Reed, B. R. Rogers, R. A. Weller, and R. D. Schrimpf, "Vanderbilt pelletron- low energy protons and other ions for radiation effects on electronics," *IEEE REDW,* 2015.

[41] E. J. Parma, G. E. Naranjo, L. L. Lippert, and D. W. Vehar, "Neutron Environment Characterization of the Central Cavity in Annular Core Research Reactor," *EPJ Web of Conferences,* 2016.

[42] M. H. Sparks, T. M. Flanders, J. G. Williams, J. G. Kelly, W. W. Sallee, M. Roknizadeh, and J. L. Meason, "Energy dependence of neutron damage in silicon bipolar transistors," *IEEE Trans. Nucl. Sci.,* vol. 36, no. 6, pp. 1904-1911, December 1989.

[43] G. C. Messenger, "A summary review of displacement damage from high energy radiation in semiconductors and semiconductor devices," *RADECS 91,* pp. 35-40, 1991.

[44] Boeing aerospace company, "Radiation and shielding study for the international ultraviolet explorer," Seattle, WA, USA., October 1974.

[45] B. G. Rax, A. H. Johnson, and T. Miyahira, "Displacement damage in bipolar linear integrated circuits," *IEEE Trans. Nucl. Sci.,* vol. 46, no. 6, pp. 1660-1665, December 1999.

[46] "E264-13: Standard test method for measuring fast-neutron reaction rates by radioactivation of nickel," *ASTM International,* 2013.

[47] "E265-15: Standard test method for measuring reaction rates and fast-neutron fluences by radioactivation of sulfur-32," *ASTM International,* 2015.

[48] "E2450: Standard Practice for Application of Thermoluminescence-Dosimetry (TLD) Systems for Determining Absorbed Dose in Radiation-Hardness Testing of Electronic Devices," *ASTM International.*

[49] E. J. Parma, T. J. Quirk, L. L. Lippert, P. J. Griffin, G. E. Naranjo, and S. M. Luker, "Radiation characterization summary: ACRR 44-inch lead-boron bucket located in the central cavity on the 32-inch pedestal at the core centerline," SAND 2013-3406, Albuquerque, NM, April 2013.

[50] GUM: Guide to the expression of uncertainty in measurement. document JCGM 100:2008, BIPM, 2008.

[51] J. R. Schwank, M. R. Shaneyfelt, P. Paillet, D. E. Beutler, V. Ferlet-Cavrois, B. L. Draper, R. A. Loemker, P. E. Dodd, and F. W. Sexton, "Optimum laboratory radiation source for hardness assurance testing," *IEEE Trans. Nucl. Sci.,* vol. 48, no. 6, pp. 2152-2157, December 2001.

[52] P. Paillet, J. R. Schwank, M. R. Shaneyfelt, V. Ferlot-Cavrois, R. L. Jones, O. Flament, E. W. Blackmore, "Comparison of charge yield in MOS devices for different radiation sources," *IEEE Trans. Nucl. Sci.,* vol. 49, no. 6, pp. 2656-2661, December 2002.

[53] S. R. Messenger, E. A. Burke, G. P. Summers, and R. J. Walters, "Limits to the application of NIEL for damage correlation," *IEEE Trans. Nucl. Sci.,* vol. 51, no. 6, pp. 3201-3206, December 2004.

[54] B. R. Gossick, "Disordered regions in semiconductors bombarded by fast neutrons," *Jour. Appl. Phys.,* vol. 30, no. 8, pp. 1214-1218, August 1959.

[55] Sandia National Laboratories Gamma Irradiation Facility [Online]. Available: http://www.sandia.gov/research/facilities/gamma_irradiation_facility.html.

[56] I. Lazanu and S. Lazanu, "The role of primary point defects in the degradation of silicon detectors due to hadron and lepton irradiation," *Phys. Scr. ,* vol. 74, pp. 201-207, 2006.